



TECHNISCHE
UNIVERSITÄT
WIEN

DIPLOMARBEIT

A real-time capable quasi-2D proton exchange membrane fuel cell model

ausgeführt zum Zwecke der Erlangung des akademischen Grades
eines Diplom-Ingenieurs

eingereicht an der TU Wien, Fakultät für Maschinenwesen und Betriebswissenschaften

von

Dominik KUZDAS

Matrikelnummer: 00925099

Schusswallgasse 3/3

1050 Wien

Dominik MURSCHENHOFER

Matrikelnummer: 00927263

Gassergasse 2-8/1/8

1050 Wien

unter der Leitung von

Ao.Univ.Prof. Dipl.-Ing. Dr.techn. Stefan BRAUN

Institut für Strömungsmechanik und Wärmeübertragung

und

Univ.Prof. Dipl.-Ing. Dr.techn. Stefan JAKUBEK

Institut für Mechanik und Mechatronik

Wien, Juli 2017


Dominik Kuzdas


Dominik Murschenhofer

EVERYTHING MUST BE MADE AS SIMPLE AS POSSIBLE.
BUT NOT SIMPLER.

Albert Einstein

I HAVE BEEN IMPRESSED WITH THE URGENCY OF DOING.
KNOWING IS NOT ENOUGH; WE MUST APPLY.
BEING WILLING IS NOT ENOUGH; WE MUST DO.

Leonardo da Vinci

Eidesstattliche Erklärung

Ich, Dominik Kuzdas, erkläre an Eides statt, dass die vorliegende Arbeit nach den anerkannten Grundsätzen der wissenschaftliche Abhandlungen von mir selbstständig erstellt wurde.

Alle verwendeten Hilfsmittel, insbesondere die zugrunde gelegte Literatur, sind in dieser Arbeit genannt und aufgelistet. Die aus den Quellen wörtlich entnommenen Stellen, sind als solche kenntlich gemacht.

Das Thema der Arbeit wurde von mir bisher weder im In- noch im Ausland einer Beurteilerin/einem Beurteiler zur Begutachtung in irgendeiner Form als Prüfungsarbeit vorgelegt. Diese Arbeit stimmt mit der von den Begutachterinnen/Begutachtern beurteilten Arbeit überein.

Wien, am 6. Juli 2017


Dominik Kuzdas

Ich, Dominik Murschenhofer, erkläre an Eides statt, dass die vorliegende Arbeit nach den anerkannten Grundsätzen der wissenschaftliche Abhandlungen von mir selbstständig erstellt wurde.

Alle verwendeten Hilfsmittel, insbesondere die zugrunde gelegte Literatur, sind in dieser Arbeit genannt und aufgelistet. Die aus den Quellen wörtlich entnommenen Stellen, sind als solche kenntlich gemacht.

Das Thema der Arbeit wurde von mir bisher weder im In- noch im Ausland einer Beurteilerin/einem Beurteiler zur Begutachtung in irgendeiner Form als Prüfungsarbeit vorgelegt. Diese Arbeit stimmt mit der von den Begutachterinnen/Begutachtern beurteilten Arbeit überein.

Wien, am 6. Juli 2017


Dominik Murschenhofer

Danksagung

Dominik Kuzdas

Ganz besonders möchte ich Prof. Stefan Braun und Prof. Stefan Jakubek danken, die mich mit unzähligen fachlichen Diskussionen durch die Diplomarbeit geleitet haben und mich auch in anstrengenden Zeiten mit persönlichen Ratschlägen ermutigten.

Weiters möchte ich mich bei meinen Eltern Brigitte und Hubert und meiner Schwester Daniela bedanken, die mir stets auf meinem Weg zur Seite standen und ohne dessen Hilfe mein Studium nicht möglich gewesen wäre.

Danken möchte ich außerdem meiner Freundin Marina S. die mein Leben seit Beginn meines Studiums bereichert.

Dominik Murschenhofer

Zuerst möchte ich mich bei Prof. Stefan Braun und Prof. Stefan Jakubek für ihre ausgiebige Unterstützung zur Erarbeitung dieser Diplomarbeit bedanken. Durch stetig kritisches Hinterfragen, konstruktive Kritik und aufmunternde Ratschläge verhalfen sie mir einen gut überlegten und strukturierten Lösungsweg zu finden.

Weiters gilt mein besonderer Dank meinen Eltern Sigrid und Michael, sowie meiner Schwester Sonja für die Geduld und Unterstützung, die sie mir während des gesamten Studiums entgegengebracht haben. Sie hatten stets ein offenes Ohr für meine Sorgen, ohne meine Familie wäre ich nie so weit gekommen.

Abstract

In this paper a dynamic proton exchange membrane fuel cell model for real-time applications is presented. Following a quasi-2D approach, effects such as multicomponent diffusion in porous layers, membrane water transport driven by diffusion and electroosmotic drag as well as membrane nitrogen crossover forced by partial pressure differences, are considered. A linearisation of the governing equations with respect to the previous time step is applied to avoid numerically expensive Newton iterations and to speed up the simulation. Furthermore, a solution method based on Chebyshev collocation minimises the required number of nodes and assures real-time capability. The model is validated in terms of polarisation curves, current density and species distribution versus steady-state computational fluid dynamics simulations of a 3D fuel cell performed in AVL FireTM. The transient behaviour is found to be in good qualitative agreement with results published by other authors. Due to the fast computation capability of the presented model, it is suitable for widespread parameter studies, control unit adjustments or state predictions, e.g. fuel starvation or membrane drying and flooding.

Kurzfassung

Diese Arbeit präsentiert ein dynamisches Protonenaustauschmembran-Brennstoffzellenmodell mit dem Schwerpunkt auf Echtzeitfähigkeit. Verschiedene physikalische Effekte wie zum Beispiel multikomponenten Diffusion in den porösen Gasdiffusionsschichten, Wassertransport durch die Protonenaustauschmembran, getrieben durch Diffusion sowie elektro-osmotische Kräfte und Stickstofftransport durch die Membran werden innerhalb einer quasi-zweidimensionalen Beschreibung berücksichtigt. Um Echtzeitfähigkeit zu erreichen wird eine Linearisierung um die Lösung des vorigen Zeitschritts angewendet, die es ermöglicht die zugrundeliegenden nichtlinearen Gleichungen ohne numerisch aufwendige Newton-Iteration zu lösen. Um die Anzahl der örtlichen Diskretisierungspunkte zu minimieren, wird eine Chebyshev-Kollokationsmethode verwendet, die bereits mit wenigen Rechenpunkten Lösungen hoher Genauigkeit liefert. Zur Validierung des Modells gegen die kommerzielle Simulationssoftware AVL FireTM werden Polarisierungskurven, die Verteilung der Stromdichte und der Spezienverläufe von stationären Zuständen betrachtet. Die charakteristische Verläufe der Stromdichte für dynamische Änderungen der Einlassfeuchte oder der Zellenspannung stimmen sehr gut mit den Ergebnissen anderer Autoren überein. Aufgrund der Echtzeitfähigkeit des Modells kann es für breit gefächerte Parameterstudien, als virtuelle Brennstoffzelle zur Reglerauslegung oder für die Vorhersage von kritischen Zuständen wie zum Beispiel Treibstoffverarmung und Membranaustrocknung oder Überflutung verwendet werden.

Contents

1	Introduction ^{DK}	1
2	Physical-mathematical model	4
2.1	Quasi-2D approach ^{DM}	6
2.2	Gas channel and GDL model ^{DK}	6
2.3	Membrane model ^{DM}	10
2.4	Electrochemical model ^{DK}	11
2.5	Coupling conditions	12
2.5.1	Interface gas channel - GDL ^{DK}	13
2.5.2	Interface GDL - membrane ^{DM}	13
2.6	Boundary conditions ^{DK}	14
3	Numerical treatment	15
3.1	Discretisation	15
3.1.1	Spatial domain ^{DM}	15
3.1.2	Time domain ^{DK}	16
3.2	Linearisation in time (LIT) ^{DK}	16
3.3	Coupling between gas channel and GDL	20
3.3.1	Evaluation of the Chebyshev polynomial ^{DK}	21
3.3.2	Implicit polynomial interpolation ^{DM}	21
4	Validation and discussion ^{DM}	23
5	Conclusion and outlook ^{DK}	35
	Nomenclature	37

Bibliography	41
Appendix A Dimensionless groups ^{DM}	45
Appendix B LIT PEMFC model - user guide	48
B.1 Input files ^{DM}	51
B.1.1 Geometry data	51
B.1.2 Material properties	51
B.1.3 Boundary conditions	53
B.2 Assistant files ^{DK}	58
B.2.1 Characteristic values	58
B.2.2 Coefficients	58
B.3 Main file ^{DM}	59
B.3.1 Load data	59
B.3.2 Assistant variables	59
B.3.3 Initial conditions	59
B.3.4 Time loop	59
B.3.5 Save results	60
B.3.6 Plot results	61
B.4 Functions ^{DK}	62
B.4.1 SystemMatrix.m	62
B.4.2 sliceCoupling.m	62
B.4.3 central_diff_t.m	62
B.4.4 bc_physical.m	63
B.4.5 Chebfun package	64

^{DK} indicates chapters formulated by Dominik Kuzdas

^{DM} indicates chapters formulated by Dominik Murschenhofer

Chapter 1

Introduction ^{DK}

Proton exchange membrane fuel cells (PEMFCs) are a promising alternative power source for mobile and stationary devices. Low operating noise, the relative simplicity due to no moving parts, zero emission of greenhouse gases and a high energy density combined with high efficiency are the main advantages. In recent decades, fundamental knowledge about fuel cell (FC) operating conditions has been gained by studying both experimental and computer simulation results. However, dynamic operation of a FC is still very challenging and the issue of reduced durability and performance occurring from unmeant destructive states is hardly tackled successfully. State-of-the-art FCs are coupled to a battery to bridge dynamic load changes and achieve almost steady working conditions. Transient operation is of high interest for next generation FCs to avoid the battery's costs and weight. Therefore, real-time control will be essential to prevent local destructive states and maintain high efficiency. To this end, a FC model based on physical grounds is desirable for affordable testing, control unit adjustment and to perform widespread parameter studies within moderate computation time.

The first FC models were presented by Bernardi and Verbrugge [1] and Springer *et al.* [2] in the early 90s. These models describe 1D mass transfer in the membrane direction and consider steady-state operation only. Springer *et al.* [2] introduced a model for the water transport across the membrane which partly is still used nowadays. A quasi-2D approach – coupling a 1D gas channel model with a 1D model for mass transport through the membrane electrode assembly – which is suitable to describe

spatial variations of current density, water distribution and membrane ohmic resistance was presented by Dannenberg *et al.* [3]. This quasi-2D description was further used by many other authors, [4, 5, 6]. While Berg *et al.* [4] presented a new approach to couple gas diffusion layers (GDLs) with the membrane considering non-equilibrium effects, Freunberger [5] and Kulikovsky [6] assumed equilibrium between the membrane water content and the GDL water vapour activity at the corresponding interface [2].

A transient 2D PEMFC model presented by Wu *et al.* [7] is also based on Springer's coupling approach and uses pure oxygen (O_2) and hydrogen (H_2) as feed gas on cathode and anode side, respectively. They developed their work further to treat non-isothermal transient 3D-effects [8] and analysed the dynamic influence of Springer's equilibrium and Berg's non-equilibrium coupling methods between GDLs and membrane. However, as their fuel cell is fed with pure O_2 , phenomena related to the presence of nitrogen (N_2), as multicomponent diffusion, N_2 membrane crossover and material properties depending on the N_2 distribution have not been taken into account. Wang and Wang [9] presented a dynamical 3D model and studied the importance of various physical effects, such as membrane hydration, GDL species transport due to diffusion and convective gas transport in the gas channels, by considering relevant time scales. The FC model is operated with humidified O_2 and H_2 and therefore only accounts for binary diffusion between fuel gas and water. Assuming isothermal cell conditions, transient simulations have been performed by using a commercial computational fluid dynamics (CFD) software. They analysed the dynamic response to step changes of cell potential and cathode inlet humidification. In their subsequent work, [10], the model was extended to include the electron transport and the response to step changes of average current density was investigated. FCs are commonly fed with humidified air and H_2 on cathode and anode side, respectively. To allow higher stoichiometry in terms of higher anode inlet velocities without wasting unconsumed H_2 , re-circulation or dead-end modes are used on the anode side. This enables nitrogen accumulation at the anode due to membrane crossover. Consequently, the N_2 distribution must be considered in the entire FC. In all these works, designed to improve the understanding of FC operation behaviour, commonly applied spatial resolution of each domain is too high to achieve moderate computation times. The loss of resolution depth is currently unavoidable to reach real-time capability.

Today, models using the built-up knowledge for fast state prediction are hardly available with acceptable accuracy since most of them suffer from oversimplification. A zero-dimensional FC-stack model presented by Pathapati *et al.* [11] may be used to predict voltage response behaviour during current load step changes. This model delivers useful information about the overall stack behaviour. However, for today's control purposes, a more detailed resolution of spatial current density and species distribution is desirable. Gao *et al.* [12] proposed a 1D model for real-time FC-stack simulation, adaptable to various stack configurations with different geometries. Their consideration of steady-state conditions in the GDLs and the membrane leads to a decrease of computation time. However, membrane hydration significantly affects the FC's dynamics and a transient treatment is desirable nowadays. A single cell model based on 2D gas channel treatment, coupled to a 1D model for GDLs and membrane, was presented by Massonnat *et al.* [13]. Real-time capability is achieved by assuming steady-state conditions in the gas channels. Nevertheless, assuming a uniformly distributed current density may also oversimplify the problem.

The current work intends to fill the gap between highly complex 3D models requiring much computational effort and fast 1D models possibly lacking of spatial resolution depth. A 'linearisation in time' (LIT) and a quasi-2D-discretisation, capturing the principal directions for mass transport and taking into account spatial distributions of species and current density without requiring excessive computational power, provide the basis of the presented LIT model. The model equations are derived from the integral conservation laws and supplemented with model equations for membrane water transport, membrane conductivity, species diffusion etc. in Sec. 2. As membrane N₂-crossover is considered to be important for present-day control issues, the distribution of N₂ and therefore multicomponent diffusion are being taken into account on both FC sides. The entire model is finally represented by a system of coupled, nonlinear partial differential equations (PDEs) which must be solved numerically. To achieve real-time capability, a linearisation of the PDEs with respect to the previous time step in the marching scheme is used. The implementations of an implicit coupling method between different spatial domains and the linearisation scheme are presented in Sec. 3. Finally, the model is validated against the commercial CFD package AVL FireTM[14] for some standard test cases and the time-dependent results are presented and discussed in Sec. 4.

Chapter 2

Physical-mathematical model

In the following, we present general assumptions, the modelled domains and their quasi-2D approach as well as models used to describe various phenomena. Moreover, the governing equations for each domain, gas channels (GC), GDLs and proton exchange membrane (PEM) are individually derived. Finally, the coupling of single domains and providing appropriate boundary conditions yield the proposed model description. The derivation of the current model development is based on the following assumptions:

1. Continuum mechanics approach in each domain.
2. At the current state the entire FC is operated at a constant temperature. However, the temperature distribution of a real FC could be easily mapped on the model in a parametric manner, as it allows locally different temperatures.
3. Gas species behave like an ideal gas mixture and its properties such as viscosity, diffusion coefficients etc. , depending on species distribution.
4. Both FC channels are fed with humidified reactant gases, O_2 and H_2 on cathode and anode, respectively and nitrogen. Consequently, multicomponent diffusion is considered on both sides.
5. Reactant crossover through the membrane is neglected.

6. GDL's ohmic resistance is neglected.

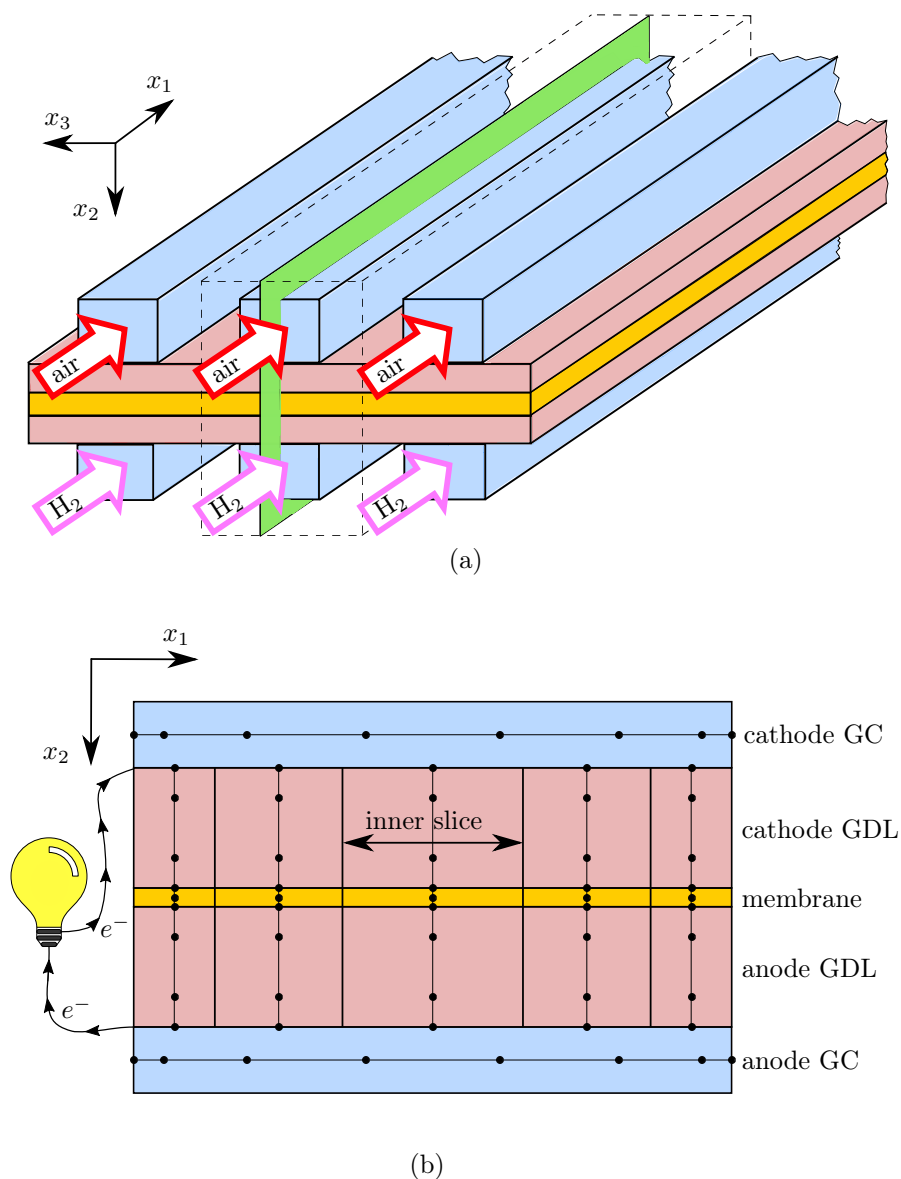


Figure 2.1: (a) 3D PEMFC geometry with the modelled domain, bounded by dashed lines and the considered 2D plane in green. (b) Discretised quasi-2D model domain with $N_{GC}^{C,A} = 8$, $N_{GDL}^{C,A} = 4$ and $N_{PEM} = 3$ computation nodes for the gas channels (GC), the GDLs and the membrane, respectively, and the number of so-called 'inner slices' $N_{SL} = 5$ (spatial resolution used for all simulations below).

2.1 Quasi-2D approach ^{DM}

In order to develop a real-time capable model with sufficient spatial resolution, a suitable defined computational domain is needed. Starting from a typical 3D description of a single cell with straight channels, a 2D domain is obtained by cutting through the channel's symmetry plane, see the green plane in Fig. 2.1(a). Further, a quasi-2D approach, presented by Dannenberg *et al.* [3], considering principle directions for gradients of corresponding variables in each domain, is applied. The 2D domain is therefore divided in two parallel gas channels connected with an arbitrary number of 'inner slices', each composed of cathode and anode GDLs and a PEM in between, see Fig. 2.1(b). For each domain a 1D formulation of the model equations is found from the integral conservation laws [15] and the application of cross-sectional averaging of the relevant variables, e.g. for the velocity profile $\tilde{u}_1(\tilde{\vec{x}}, \tilde{t})$ with $\tilde{\vec{x}} = (\tilde{x}_1, \tilde{x}_2, \tilde{x}_3)^T$ in the gas channels,

$$\tilde{u}_1(\tilde{x}_1, \tilde{t}) = \frac{1}{\tilde{H}_{GC}\tilde{W}_{GC}} \int_0^{\tilde{H}_{GC}} \int_0^{\tilde{W}_{GC}} \tilde{u}_1(\tilde{\vec{x}}, \tilde{t}) \, d\tilde{x}_2 \, d\tilde{x}_3. \quad (2.1)$$

Here, $\tilde{u}(\tilde{x}_1)$ is the required quantity (velocity) to be determined, and $\tilde{W}_{GC}\tilde{H}_{GC}$ is the constant cross-sectional area. Further, tilde denotes a dimensional variable, whereas no tilde represents the corresponding dimensionless quantity (see Appendix A for details). Consequently, variations along the \tilde{x}_1 -direction are considered for the gas channels, and variables in the GDLs and membrane depend on \tilde{x}_2 , only. Hence, inner slices are connected via the gas channels only, see Fig. 2.1(b).

2.2 Gas channel and GDL model ^{DK}

The gas channel flow turns out to be laminar in general, is assumed to be locally fully developed and thus governed by a parabolic velocity profile [16], even though mass and momentum are exchanged with the GDL, see Fig. 2.2(a).

For the gas channel model, the integral formulation of the conservation of mass for a control volume $\tilde{C}\tilde{V}$ containing the entire channel height and width in \tilde{x}_2 and \tilde{x}_3 -

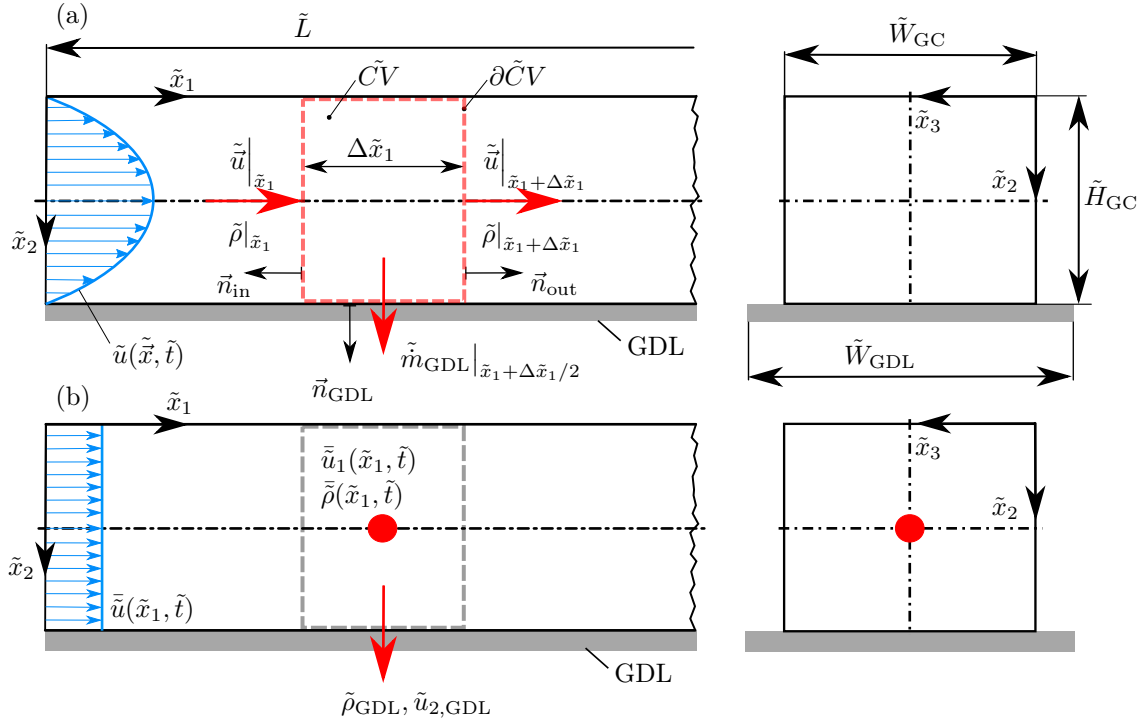


Figure 2.2: Velocity distribution in the gas channel model, whereas (a) displays the parabolic velocity distribution before cross-sectional averaging is applied and variables depend on \tilde{x}_1 - and \tilde{x}_2 -direction, (b) represents the quasi-1D formulation with the cross-sectional averaged variables.

direction, respectively, and an channel length element $\Delta\tilde{x}_1$ in \tilde{x}_1 -direction with $\frac{\Delta\tilde{x}_1}{L} \ll 1$, [see red dashed rectangle in Fig. 2.2(a)] reads:

$$\int_{\tilde{C}\tilde{V}} \frac{\partial \tilde{\rho}(\tilde{x}, \tilde{t})}{\partial \tilde{t}} d\tilde{V} + \oint_{\partial \tilde{C}\tilde{V}} \tilde{\rho}(\tilde{x}, \tilde{t}) \tilde{u}(\tilde{x}, \tilde{t}) \cdot \tilde{n} d\tilde{S} = 0. \quad (2.2)$$

Here, $\partial \tilde{C}\tilde{V}$ denotes the closed control volume surface. Whereas the first term represents the change of mass within the control volume with respect to time, the second term represents the channel mass flux $\tilde{\rho}\tilde{u}_1$ along the \tilde{x}_1 -direction and the mass transport at the gas channel - GDL interface $\tilde{\rho}\tilde{u}_2$ along the \tilde{x}_2 direction, depicted by the red arrows in Fig. 2.2. A formulation with dependency in \tilde{x}_1 -direction only is obtained by substituting the variables $\tilde{\rho}(\tilde{x}, \tilde{t})$ and $\tilde{u}(\tilde{x}, \tilde{t})$ with the corresponding cross-sectional averaged values $\tilde{u}(\tilde{x}_1, \tilde{t})$ and $\tilde{\rho}(\tilde{x}_1, \tilde{t})$ using Eq. (2.1). However, the mass flux at the

GDL interface is determined from the GDL model:

$$\tilde{m}_{\text{GDL}}(\tilde{x}, \tilde{t}) = \Delta\tilde{x}_1 \tilde{W}_{\text{GDL}} \tilde{\rho}_{\text{GDL}}(\tilde{x}_1, \tilde{H}_{\text{GC}}, \tilde{t}) \tilde{u}_{2,\text{GDL}}(\tilde{x}_1, \tilde{H}_{\text{GC}}, \tilde{t}). \quad (2.3)$$

Evaluating the surface integral in Eq. (2.2), using Eq. (2.3) and a Taylor series expansion, the integral conservation of mass for cross-sectional averaged variables reads:

$$\begin{aligned} 0 = & \Delta\tilde{x}_1 \tilde{W}_{\text{GC}} \tilde{H}_{\text{GC}} \frac{\partial \bar{\rho}(\tilde{x}_1, \tilde{t})}{\partial \tilde{t}} \\ & + \Delta\tilde{x}_1 \tilde{W}_{\text{GDL}} \tilde{\rho}_{\text{GDL}}(\tilde{x}_1, \tilde{H}_{\text{GC}}, \tilde{t}) \tilde{u}_2(\tilde{x}_1, \tilde{H}_{\text{GC}}, \tilde{t}) \\ & + \Delta\tilde{x}_1 \tilde{W}_{\text{GC}} \tilde{H}_{\text{GC}} \frac{\partial (\bar{\rho}(\tilde{x}_1, \tilde{t}) \bar{u}_1(\tilde{x}_1, \tilde{t}))}{\partial \tilde{x}_1} + \mathcal{O} \left(\left(\frac{\Delta\tilde{x}_1}{\tilde{L}} \right)^2 \right). \end{aligned} \quad (2.4)$$

The differential form for the quasi-1D conservation of mass characterised by Fig. 2.2(b) is finally found by letting $\Delta\tilde{x}_1 \rightarrow 0$:

$$\frac{\partial \bar{\rho}}{\partial \tilde{t}} + \frac{\partial (\bar{\rho} \bar{u}_1)}{\partial \tilde{x}_1} = - \frac{\tilde{W}_{\text{GDL}}}{\tilde{W}_{\text{GC}}} \frac{1}{\tilde{H}_{\text{GC}}} \tilde{\rho}_{\text{GDL}} \tilde{u}_{2,\text{GDL}}. \quad (2.5)$$

To express the wall shear stress $\tilde{\tau}_w$ at the solid channel walls in the conservation law of momentum in terms of the Darcy-Weisbach friction factor f_D depending on the gas channel's width and height, the hydraulic diameter \tilde{D}_H – defined as the ratio between the channel cross section and the cross section's wetted perimeter – is introduced [17],

$$\tilde{\tau}_w = \tilde{\rho} \tilde{u}^2 \frac{f_D}{8}, \quad f_D = \frac{64 \tilde{\mu}}{\tilde{\rho} \tilde{u} \tilde{D}_H} F_c, \quad \tilde{D}_H = \frac{2 \tilde{H} \tilde{W}}{\tilde{H} + \tilde{W}}. \quad (2.6)$$

Here, $\tilde{\mu}$ denotes the ideal gas mixture's dynamic viscosity, depending on gas composition [18]. Since the concept of the hydraulic diameter is known to be inaccurate for laminar flows, a correction factor F_c is used [15].

In the gas channels, diffusive fluxes are found to be negligibly small in contrast to convective fluxes. However, in the GDLs both convective and diffusive mass transports are accounted for, whereas the latter is modelled with generalised Fick's law of diffusion. For multicomponent diffusion with three species, two diffusive species fluxes read in

dimensionless form [19]:

$$j_\alpha = -\rho\varepsilon^q \left(\mathcal{D}_{\alpha,\alpha} \frac{\partial \xi_\alpha}{\partial x_2} + \mathcal{D}_{\alpha,\beta} \frac{\partial \xi_\beta}{\partial x_2} \right), \quad \alpha \neq \beta, \quad (2.7)$$

whereas the third flux is used to close the system,

$$\sum_{\gamma} j_\gamma = 0. \quad (2.8)$$

The indices α, β and γ are listed in Table 2.1. Here, the generalised dimensionless diffusion coefficients $\mathcal{D}_{\alpha,\alpha}$ and $\mathcal{D}_{\alpha,\beta}$ (reference values are given in Table A.1) are related to mass fractions [20] and are computed based on a model for binary diffusion coefficients [21]. In order to consider the porosity ε of the GDLs, Darcy's law and the specific value for the Bruggeman exponent $q = 1.5$ are used [22].

Analogous to the derivation of the differential form of the conservation of mass in the gas channel, Eqs. (2.1-2.5), the differential forms for the conservation of momentum and species can be found. Additionally, introducing characteristic reference quantities (see Table A.1), the dimensionless form of the governing equations for the gas channel ($a = 1$) and the GDL ($a = 2$) read:

$$\text{mass:} \quad \frac{\partial \rho}{\partial t} + \frac{\partial(\rho u_a)}{\partial x_a} = S_m, \quad (2.9)$$

$$\text{momentum:} \quad \rho \frac{\partial u_a}{\partial t} + \rho u_a \frac{\partial u_a}{\partial x_a} + K_{p,a} \frac{\partial p}{\partial x_a} = S_u, \quad (2.10)$$

$$\text{species:} \quad \rho \frac{\partial \xi_\alpha}{\partial t} + \rho u_a \frac{\partial \xi_\alpha}{\partial x_a} = S_s, \quad (2.11)$$

where the explicit expressions for the source terms $S_{m,u,s}$ are summarised in Table 2.1. These four coupled nonlinear PDEs Eqs. (2.9-2.11) contain six unknowns in each domain, the velocity u_a , the pressure p , the density ρ and the three mass fractions ξ_γ with $\gamma = \text{N}_2, \text{H}_2\text{O}$ and O_2 or H_2 on cathode or anode side, respectively. To solve for the six unknowns, two additional equations are required to close the system. Therefore, the algebraic closure equation for mass fractions and the algebraic equation of state for

an ideal gas mixture are used:

$$\text{closure equation: } \sum_{\gamma} \xi_{\gamma} = 1, \quad (2.12)$$

$$\text{equation of state: } K_{e,a} \rho \sum_{\gamma} \frac{\xi_{\gamma}}{\mathcal{M}_{\gamma}} = p. \quad (2.13)$$

The dimensionless groups $K_{p,a}$ and $K_{e,a}$ are defined in Appendix A.

source terms	gas channels	gas diffusion layers
S_m	$-K_1 \rho u_2$	0
S_u	$\mu K_2 u_1$	$\mu \left(K_4 \frac{\partial^2 u_2}{\partial x_2^2} - \varepsilon K_5 u_2 \right)$
S_s	$-K_3 j_{\alpha}$	$-\frac{1}{\varepsilon} \frac{\partial j_{\alpha}}{\partial x_2}$
species subscript	cathode	anode
α, β	O_2, H_2O	H_2, H_2O
γ	O_2, N_2, H_2O	H_2, N_2, H_2O

Table 2.1: Source terms and species indices for the corresponding domain. The definitions of the dimensionless groups $K_1 \div K_5$ are given in Appendix A.

2.3 Membrane model ^{DM}

Within the membrane, water transport is driven by three different mechanisms, namely electro-osmotic drag, proportional to the current density \tilde{i} , diffusion due to concentration gradients and convective transport caused by pressure differences [22]. The latter is neglected as it plays a minor role for FC applications [23] and the membrane water flux \tilde{j}_w reads [22, 24],

$$\tilde{j}_w = -\tilde{\mathcal{M}}_{H_2O} \left(C_{\text{drag}}(\lambda) \frac{\tilde{i}}{\tilde{F}} + \frac{\tilde{\rho}_{\text{PEM}}}{\tilde{E}\tilde{W}} \tilde{D}_w(\lambda) \frac{\partial \lambda}{\partial \tilde{x}_2} \right). \quad (2.14)$$

The coefficients for electro-osmotic drag C_{drag} and back diffusion \tilde{D}_w are functions of the normalised membrane water content λ , [24], defined as number of water molecules

per sulfonic acid groups present in the polymer, $\lambda = n_{\text{H}_2\text{O}}/n_{\text{SO}_3\text{H}}$.

By means of characteristic reference quantities, the dimensionless form of the normalised membrane water content transport equation yields

$$\frac{\partial \lambda}{\partial t} = K_6 \frac{\partial \lambda}{\partial x_2} i + \left[\left(\frac{\partial \lambda}{\partial x_2} \right)^2 + \lambda \frac{\partial^2 \lambda}{\partial x_2^2} \right], \quad (2.15)$$

where the dimensionless group K_6 is defined in Appendix A.

As the normalised membrane water content is the only variable considered in the membrane, there are no additional equations required within this domain. However, besides for water, the membrane is also permeable for N_2 with the concentration gradient (which, according to Henry's law, is proportional to the partial pressure gradient [23]) as driving force. A linear distribution of N_2 across the PEM can be assumed [25], i.e. the crossover flux $\tilde{j}_{\text{N}_2}^{\text{cross}}$ appears as coupling condition at the GDL - membrane interface [see Eq. (2.22)] only,

$$\tilde{j}_{\text{N}_2}^{\text{cross}} = \tilde{\mathcal{M}}_{\text{N}_2} \tilde{k}_{\text{N}_2}(\lambda) \frac{\tilde{p}_{\text{N}_2}^{\text{C}} - \tilde{p}_{\text{N}_2}^{\text{A}}}{\tilde{H}_{\text{PEM}}}. \quad (2.16)$$

Here, $\tilde{p}_{\text{N}_2}^{\text{C}}$ and $\tilde{p}_{\text{N}_2}^{\text{A}}$ denote the nitrogen partial pressure at the cathode and anode GDL - membrane interface, respectively. The nitrogen permeance \tilde{k}_{N_2} depends on the membrane water content λ . For a device temperature of $\tilde{T} = 343.15\text{K}$ the quadratic relation presented by Ahluwalia and Wang [26] is approximated by a line of best fit,

$$\tilde{k}_{\text{N}_2} = (0.2517 + 0.0373\lambda) \times 10^{-12} \left[\frac{\text{mol}}{\text{s m Pa}} \right]. \quad (2.17)$$

2.4 Electrochemical model ^{DK}

The cell potential \tilde{E}_{cell} is computed by subtracting the losses from the open-circuit cell potential \tilde{E}_{OC} ,

$$\tilde{E}_{\text{cell}} = \tilde{E}_{\text{OC}} - \tilde{i} \int_0^{\tilde{H}_{\text{PEM}}} \frac{d\tilde{x}_2}{\tilde{\sigma}(\lambda)} - \frac{\tilde{R}\tilde{T}}{\alpha_c \tilde{F}} \ln \left(\frac{\tilde{i}}{\tilde{i}_0} \right), \quad (2.18)$$

with the exchange current density \tilde{i}_0 defined as [22]

$$\tilde{i}_0 = \tilde{i}_{0,r} \tilde{\alpha}_c \tilde{L}_c \left(\frac{\tilde{p}_{\text{O}_2}}{\tilde{p}_{\text{O}_2,r}} \right)^{\gamma_c} \exp \left[\frac{-\tilde{E}_{\text{act}}}{\tilde{R}\tilde{T}} \left(1 - \frac{\tilde{T}}{\tilde{T}_{0,r}} \right) \right]. \quad (2.19)$$

In Eq. (2.18), the second and the third term on the right-hand side represent the ohmic loss due to membrane conductivity and the cathode activation polarisation loss, respectively. Because of the sluggish oxygen reduction, the polarisation losses at the anode side are negligibly small [22, 27]. The concentration polarisation losses on both sides are neglected since they play a role for high current densities only.

For a constant device temperature, the ionic conductivity $\tilde{\sigma}$ used in Eq. (2.18) depends linearly on the membrane water content [2],

$$\tilde{\sigma} = (-0.326f_1 + 0.5139f_2 \lambda) \exp \left(\frac{1286}{303} - \frac{1286\text{K}}{\tilde{T}} \right) \left[\frac{\text{S}}{\text{m}} \right]. \quad (2.20)$$

The parameters α_c , $\tilde{i}_{0,r} \tilde{\alpha}_c \tilde{L}_c$, γ_c , f_1 and f_2 in Eqs. (2.18), (2.19) and (2.20) can be used to fit the LIT model to an individual FC.

2.5 Coupling conditions

The gas channel and GDL models on cathode and anode side are each governed by a system of six coupled equations, four differential Eqs. (2.9-2.11), and two algebraic Eqs. (2.12-2.13), the membrane water transport model and the electro-chemical model are governed by one partial differential Eq. (2.15) and one algebraic Eq. (2.18), respectively. In total, this results in 26 equations for 26 unknowns, valid in different domains, which must be merged by appropriate coupling conditions.

2.5.1 Interface gas channel - GDL ^{DK}

At the gas channel - GDL interface, the variable values and the appearing fluxes are coupled. At the cathode and the anode side, the corresponding values for the pressure, the density and the mass fractions are equal:

$$\tilde{p}_{GC} = \tilde{p}_{GDL}, \quad \tilde{\rho}_{GC} = \tilde{\rho}_{GDL}, \quad \xi_{\alpha,GC} = \xi_{\alpha,GDL}. \quad (2.21)$$

The quasi-1D gas channel model already considers coupling fluxes at the interface due to the integral formulation. The mass fluxes ρu_2 and j_α appear in the source terms $S_{m,s}$, in Eqs. (2.9,2.11). Even though a quasi-2D description is used, different gas channel and GDL widths in x_3 -direction [see Fig. 2.1(a)] are considered by scaling the exchange fluxes with the ratio of the widths $\tilde{W}_{GDL}/\tilde{W}_{GC}$, see Table 4.3.

2.5.2 Interface GDL - membrane ^{DM}

The catalyst layers are assumed to be infinitely thin and therefore the source terms accounting for the electrochemical half-reactions appear in the GDL boundary layer connected to the PEM. The coupling conditions are formulated using the conservation of total species fluxes and assuming there is no convective flow through the PEM. The specific coupling conditions for the cathode and the anode fluxes read:

$$\begin{aligned} \text{cathode: } \tilde{j}_{O_2}^{\text{tot}} &= \frac{\tilde{i}\tilde{\mathcal{M}}_{O_2}}{4\tilde{F}}, \quad \tilde{j}_{N_2}^{\text{tot}} = \tilde{j}_{N_2}^{\text{cross}}, \quad \tilde{j}_{H_2O}^{\text{tot}} = \tilde{j}_w - \frac{\tilde{i}\tilde{\mathcal{M}}_{H_2O}}{2\tilde{F}}, \\ \text{anode: } \tilde{j}_{H_2}^{\text{tot}} &= -\frac{\tilde{i}\tilde{\mathcal{M}}_{H_2}}{2\tilde{F}}, \quad \tilde{j}_{N_2}^{\text{tot}} = \tilde{j}_{N_2}^{\text{cross}}, \quad \tilde{j}_{H_2O}^{\text{tot}} = -\tilde{j}_w. \end{aligned} \quad (2.22)$$

Where $\tilde{j}_\gamma^{\text{tot}} = \tilde{j}_\gamma + \tilde{\rho}_\gamma \tilde{u}$ denotes the sum of diffusive and convective species flux.

The membrane coupling conditions can be obtained via two different methods. First, by assuming water equilibrium at the GDL and PEM interface. Therefore, a semi-empirical polynomial fit, proposed by Springer *et al.* [2], is used to relate the membrane

water content λ to the GDL water vapour activity $a_w = p_{\text{H}_2\text{O}}/p_{\text{H}_2\text{O}}^{\text{sat}}$,

$$\lambda = 0.043 + 17.81a_w - 39.85a_w^2 + 36.0a_w^3. \quad (2.23)$$

The normalised membrane water content, computed with Eq. (2.23), is used directly as Dirichlet boundary condition on both membrane interfaces.

The second coupling method is based on a non-equilibrium transport model presented by Berg *et al.* [4]. Here, the water flux at the interface is assumed to be proportional to the difference between the actual membrane water content λ_a and the equilibrium membrane water content λ at the membrane - GDL interface,

$$\tilde{j}_w = \tilde{\gamma}_w (\lambda_a - \lambda). \quad (2.24)$$

The equilibrium water content λ is again computed with Eq. (2.23). However, the value of the transport coefficient $\tilde{\gamma}_w$ is not known but influences the entire dynamics of FCs significantly [8]. Therefore, the equilibrium model, Eq. (2.23), is used for the upcoming validation presented in Sec. 4. Nevertheless, the LIT model also allows the use of the non-equilibrium coupling method, Eq. (2.24).

2.6 Boundary conditions ^{DK}

Different operating modes can be obtained, depending on the applied set of boundary conditions. A mass driven model is obtained by defining the gas composition in terms of mass fractions ξ_α and the velocity $\tilde{u}_{1,\text{in}}$ at the channel inlet as well as the ambient pressure \tilde{p}_{amb} at the channel outlet, on both cathode and anode side.

Alternatively, a pressure-driven model is achieved by replacing the inlet velocity with the pressure at the channel inlet.

For the electrochemical model, a uniform potential distribution at the catalyst layers \tilde{E}_{cell} is applied as boundary condition.

Chapter 3

Numerical treatment

This section covers the numerical treatment of the presented LIT model in Matlab[®], [28], i.e. the discretisation of the spatial and the temporal domains as well as the application of a linearisation scheme to obtain a linear system of equations. To enhance the flexibility of the model, an implicit coupling method connecting the channels and the GDLs allows to choose the number of inner slices independently from the channel nodes.

3.1 Discretisation

3.1.1 Spatial domain ^{DM}

The spatial domains are treated with spectral methods; here a continuous solution is sought in terms of a Chebyshev polynomial by finding the function values of the polynomial at the nodes [29]. Spectral methods provide a high accuracy with a comparatively small number of computation nodes. To avoid spurious oscillations caused by higher order polynomial interpolation, increased node densities at the boundaries are necessary. Gauss-Lobatto points, $x_i = \cos(i\pi/N)$, $i = 0, \dots, N$ with the number of nodes N , satisfy this request and are used to discretise all domains of the LIT model. Spatial derivatives at the discrete Gauss-Lobatto points x_i of an arbitrary function $f(x)$ with

$f(x_i) = f_i$ can be found by multiplying the function with the analytically determined, dense differentiation matrix, e.g. for the first order derivative $D_{ij}^{(1)}$,

$$f'_i = \sum_j D_{ij}^{(1)} f_j. \quad (3.1)$$

The entries of the differentiation matrix $D_{ij}^{(1)}$ can be easily computed by means of the open source package `chebfun` [30]. As indicated in Fig. 2.1(b), the discretisation of all domains (channels, GDLs, membrane) and the number of inner slices can be chosen independently according to the desired resolution depth. Moreover, a Gauss-Lobatto distribution of slices in x_1 -direction is favourable to avoid oscillations due to the polynomial interpolation coupling method, see Sec. 3.3.2.

3.1.2 Time domain ^{DK}

The time derivatives are approximated by a finite difference scheme of second order accuracy, which is capable of variable time stepping, [31],

$$\left(\frac{\partial s}{\partial t}\right)^{(n+1)} = \frac{(1 + 2\alpha)s^{(n+1)} - (1 + \alpha)^2 s^{(n)} + \alpha^2 s^{(n-1)}}{(1 + \alpha)\Delta t^{(n+1)}} + \mathcal{O}(\Delta t^2). \quad (3.2)$$

Here the superscripts (n) and $(n + 1)$ denote the previous and the current instant of time, respectively, and α is defined as the current time step ratio $\alpha = \Delta t^{(n+1)}/\Delta t^{(n)}$. To adapt the time step $\Delta \tilde{t}$ within a range of $\Delta \tilde{t} = 0.001\text{s} \div 0.035\text{s}$, the rate of change between two time steps of the current density and the membrane water content is used, i.e. strong current density or membrane water content time gradients lead to a decreasing time step.

3.2 Linearisation in time (LIT) ^{DK}

As shown in Sec. 2, a system of coupled nonlinear partial differential and algebraic equations has to be solved at each time step. Aiming at real-time capability, nonlinear

terms cannot be treated with numerically expensive iterations. Therefore, a linearisation with respect to the previous time step, based on Taylor series expansion, [32], is applied. This scheme operates with the same truncation error $\mathcal{O}(\Delta t^2)$ as the approximated time derivative, Eq. (3.2). For a quadratic term su with respect to the current time step ($n+1$) the scheme yields three terms – two linear terms evaluated at the current time step and one evaluated at the previous time step (n),

$$\begin{aligned}
 s^{(n+1)}u^{(n+1)} &= \left[s^{(n)} + \left(\frac{\partial s}{\partial t} \right)^{(n)} \Delta t + \mathcal{O}(\Delta t^2) \right] \left[u^{(n)} + \left(\frac{\partial u}{\partial t} \right)^{(n)} \Delta t + \mathcal{O}(\Delta t^2) \right] \\
 &= s^{(n)}u^{(n)} + u^{(n)} \left[s^{(n)} + \left(\frac{\partial s}{\partial t} \right)^{(n)} \right] + s^{(n)} \left[u^{(n)} + \left(\frac{\partial u}{\partial t} \right)^{(n)} \right] - 2s^{(n)}u^{(n)} + \mathcal{O}(\Delta t^2) \\
 &= u^{(n)}s^{(n+1)} + u^{(n+1)}s^{(n)} - u^{(n)}s^{(n)} + \mathcal{O}(\Delta t^2) .
 \end{aligned} \tag{3.3}$$

Here, terms with respect to the current time step are highlighted in red. Applying this linearisation scheme, the approximation of the time derivative, Eq. (3.2), and the differentiation matrix [see Eq. (3.1)], e.g. the dimensionless conservation of mass derived in Sec. 2.2 reads:

$$\begin{aligned}
 \frac{3\rho_i^{(n+1)} - 4\rho_i^{(n)} + \rho_i^{(n-1)}}{2\Delta t} + \sum_{j=1}^{N_{ca}} D_{ij}^{(1)} \left(u_{1,j}^{(n+1)} \rho_j^{(n)} + u_{1,j}^{(n)} \rho_j^{(n+1)} - u_{1,j}^{(n)} \rho_j^{(n)} \right) = \\
 - \frac{W_{GDL}}{W_{GC}} \frac{1}{H_{GC}} \left[u_{2,i}^{(n+1)} \rho_i^{(n)} + u_{2,i}^{(n)} \rho_i^{(n+1)} - u_{2,i}^{(n)} \rho_i^{(n)} \right] .
 \end{aligned} \tag{3.4}$$

Here red coloured terms again denote variables with respect to the actual instant of time.

The final linear system of equations

$$\mathbf{A}\vec{x} = \vec{b}, \tag{3.5}$$

for the entire FC model is obtained by systematic application of Eqs. (3.1-3.3) to all

terms of the governing Eqs. (2.9-2.20) and the coupling conditions, Eqs. (2.21-2.23).

For transient simulations of the PEMFC, for each time step the system matrix \mathbf{A} and the right-hand side vector \vec{b} have to be updated and the system has to be solved in an implicit manner. The vector \vec{x} represents the unknown variables at the grid points, mentioned in Sec. 2.2 and 2.3,

$$\vec{x} = \begin{pmatrix} \vec{x}_{GC}^C \\ \vec{x}_{GC}^A \\ \vec{x}_{GDL,1}^C \\ \vec{x}_{PEM,1} \\ \vec{x}_{GDL,1}^A \\ i_{cur,1} \\ \vec{x}_{GDL,2}^C \\ \vec{x}_{PEM,2} \\ \vec{x}_{GDL,2}^A \\ i_{cur,2} \\ \vdots \\ \vec{x}_{GDL,n}^C \\ \vec{x}_{PEM,n} \\ \vec{x}_{GDL,n}^A \\ i_{cur,n} \end{pmatrix}, \quad \vec{x}_{GC}^C = \begin{pmatrix} u_{1,1} \\ \vdots \\ u_{1,n} \\ x_{H_2O,1} \\ \vdots \\ x_{H_2O,n} \\ \vdots \\ p_1 \\ \vdots \\ p_n \\ \rho_1 \\ \vdots \\ \rho_n \end{pmatrix}, \quad \vec{x}_{GDL,1}^C = \begin{pmatrix} u_{2,11} \\ \vdots \\ u_{2,1n} \\ x_{H_2O,11} \\ \vdots \\ x_{H_2O,1n} \\ \vdots \\ p_{11} \\ \vdots \\ p_{1n} \\ \rho_{11} \\ \vdots \\ \rho_{1n} \end{pmatrix}, \quad \vec{x}_{PEM,1} = \begin{pmatrix} \lambda_{11} \\ \vdots \\ \lambda_{1n} \end{pmatrix}.$$

Plotting the structure of the sparse matrix \mathbf{A} in Fig. 3.1, the single domains can be identified as bordered blocks along the principal diagonal and the coupling conditions between the domains can be found at the minor diagonals. The dimension N_A of the square matrix \mathbf{A} is given by,

$$N_A = N_u (N_{GC}^C + N_{GC}^A) + N_{SL} [N_u (N_{GDL}^C + N_{GDL}^A) + N_{PEM} + 1], \quad (3.6)$$

where N_{GC} , N_{GDL} , N_{PEM} denote the number of nodes in the corresponding domain, N_{SL} the number of slices and $N_u = 6$ the number of unknown variables for each grid point. Adding 1 within the squared bracket takes into account that the unknown current density appears only once per inner slice. For the discretisation, which is shown in Fig. 2.1(b) and further used to validate the LIT model, the square matrix \mathbf{A} is of dimension $N_A \times N_A = 356^2$ with a sparsity of 0.9675 (density 0.0325).

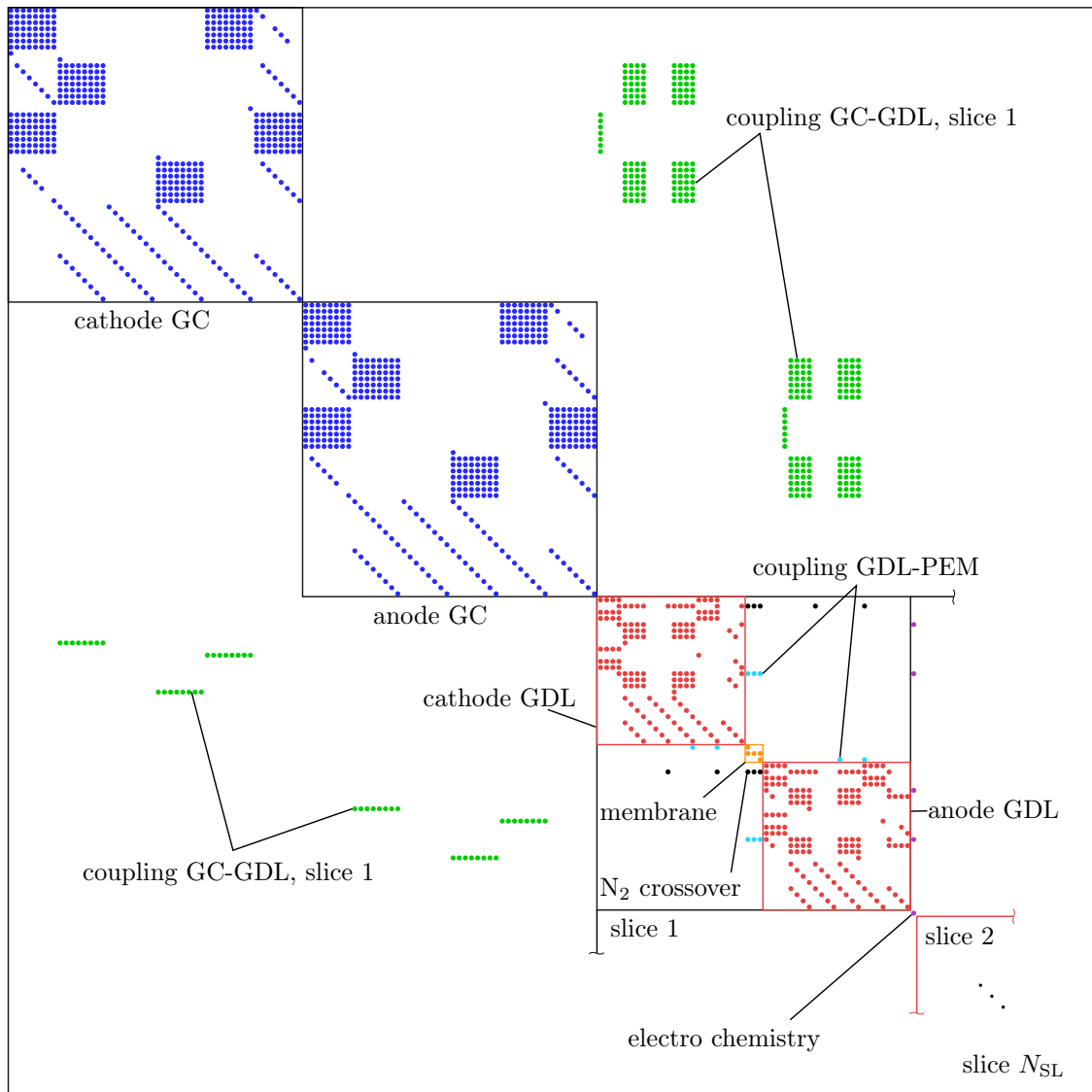


Figure 3.1: Structure of the sparse system matrix \mathbf{A} as provided by the Matlab[®] command `spy(A)`. Identification of the domains: cathode and anode channel (blue) and inner slices containing GDLs (red), PEM (orange) and the equation for electro chemistry (purple). Coupling: channel - GDL interface (green), GDL - membrane interface (cyan), N_2 crossover (black).

To avoid the nonlinearity appearing e.g. in the computation of the species depending mixture viscosity [18] and diffusion coefficients [20], such values are taken from the previous time step. This simplification is justified due to small material property alterations with respect to time. Moreover, the cubic relation for the membrane water sorption isotherm Eq. (2.23) is approximated by four lines of best fit for the range of

$0 \leq a_w < 1$ (see Fig. 3.2) and kept constant for the region of a fully saturated membrane ($a_w \geq 1$),

$$\lambda = \begin{cases} 9.879a_w + 0.342, & 0 \leq a_w < 0.199 \\ 4.120a_w + 1.490, & 0.199 \leq a_w < 0.596 \\ 14.051a_w - 4.426, & 0.596 \leq a_w < 0.798 \\ 35.768a_w - 21.752, & 0.798 \leq a_w < 1.0 \\ 14.0, & a_w \geq 1.0. \end{cases} \quad (3.7)$$

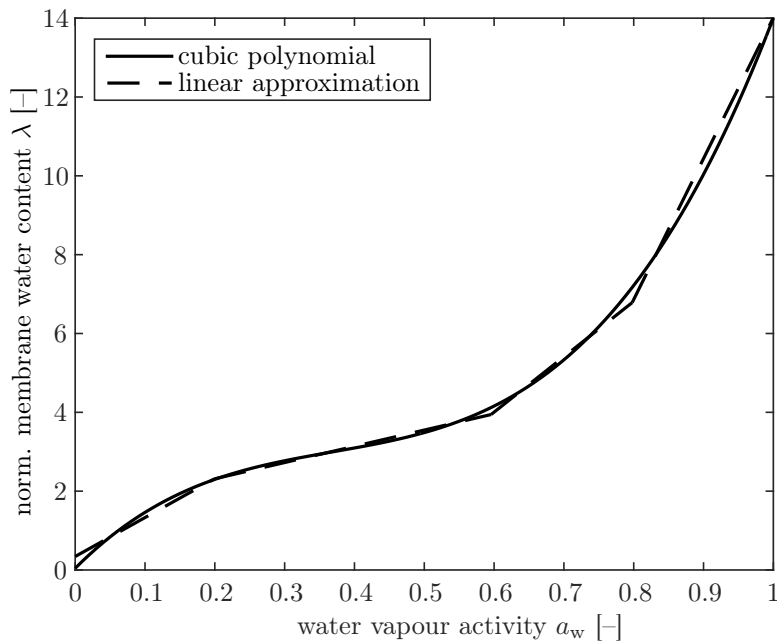


Figure 3.2: Linear approximation of Eq. (2.23) for the membrane water sorption isotherm, by four lines of constant slope, Eq. (3.7).

3.3 Coupling between gas channel and GDL

To implement the coupling conditions, presented in Sec. 2.5.1 and to achieve independent discretisation such that the number of slices do not need to coincide with the channel nodes, a two-way coupling method is applied.

3.3.1 Evaluation of the Chebyshev polynomial ^{DK}

Spectral methods offer the possibility of evaluating the underlying Chebyshev polynomial at arbitrary positions [33]. Thus, variable values are known not only at each node, but everywhere in the corresponding domain. Therefore, implicitly evaluating the Chebyshev polynomial for the quantity at each slice position in the channel provides the coupling conditions for the differential equations of the GDL model, shown in Eq. (2.21).

3.3.2 Implicit polynomial interpolation ^{DM}

The gas channel source terms shown in Table 2.1 contain the GDL fluxes, e.g. ρu_2 or j_α in order to couple channel and GDL. The governing equations for the channel are solved for each channel node and the corresponding GDL flux terms (ρu_2 , j_α , etc.) have to be determined, even though they are not explicitly known for these positions. Therefore, an interpolation polynomial,

$$p_{\text{int}}^{(n+1)}(x_1) = \sum_{i=1}^{N_{\text{SL}}} a_i^{(n+1)} x_1^{i-1} \quad (3.8)$$

of order N_{SL} , with the number of slices N_{SL} , is expanded in an implicit manner. The coefficients $a_i^{(n+1)}$ are determined by

$$a_i^{(n+1)} = \sum_{j=1}^{N_{\text{SL}}} V_{ij}^{-1} f_j^{(n+1)}, \quad (3.9)$$

where V_{ij} and $f_j^{(n+1)}$ denote the Vandermonde matrix and the GDL flux at the interface to the gas channel, respectively. The averaged flux $F_k^{(n+1)}$ for the corresponding gas channel node $k = 1, \dots, N_{\text{GC}}$, is obtained by integrating the interpolation polynomial

over the channel cell width $\Delta x_{1,k} = x_{1,k+1} - x_{1,k}$,

$$\begin{aligned}
 F_k^{(n+1)} &= \frac{1}{\Delta x_{1,k}} \int_{x_{1,k}}^{x_{1,k+1}} p_{\text{int}}^{(n+1)}(x_1) dx_1 = \sum_{j=1}^{N_{\text{SL}}} \left[\sum_{i=1}^{N_{\text{SL}}} \frac{x_{1,k+1}^i - x_{1,k}^i}{i \Delta x_{1,k}} V_{ij}^{-1} \right] f_j^{(n+1)} \\
 &= \sum_{j=1}^{N_{\text{SL}}} B_{kj} f_j^{(n+1)}.
 \end{aligned} \tag{3.10}$$

Since the entries of B_{kj} are constant in time, they can be computed in a pre-processing step and act as coefficients embedded in the matrix \mathbf{A} in Eq. (3.5).

Chapter 4

Validation and discussion ^{DM}

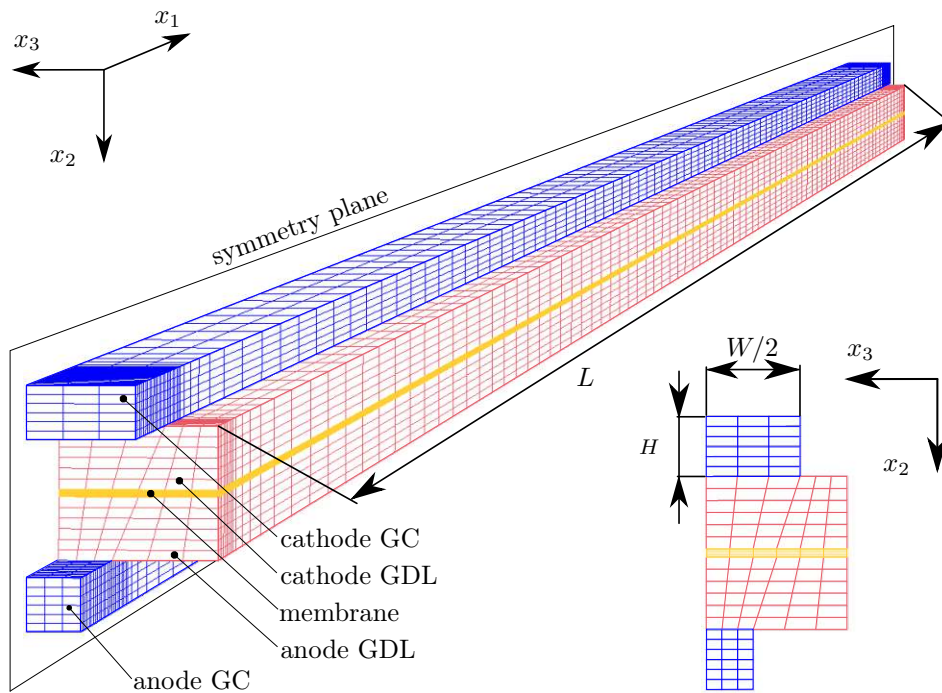


Figure 4.1: Computational domain used for 3D PEMFC simulations in AVL FireTM with a total number of 23207 cells.

The presented LIT model implemented in Matlab[®], [28], is validated against 3D simulations performed with the well-established commercial CFD package AVL FireTM, [14]. Overall predictive capabilities are presented in terms of polarisation curves and the accuracy of spatial distributions of current density and species is discussed for

selected steady-state operating points. To investigate the transient behaviour, the current density responses to changes of relative humidity at the inlet and cell potential are analysed.

Discretised domains for the LIT model and the 3D simulations are displayed in Fig. 2.1(b) and Fig. 4.1, respectively. The LIT model discretisation of $N_{GC}^{C,A} = 8$, $N_{GDL}^{C,A} = 4$, $N_{PEM} = 3$ and $N_{SL} = 5$ was chosen to assure real-time capability during all presented simulations. Furthermore, a grid convergence study resulted in this discretisation as best compromise between accuracy and computation time. To minimise the computational effort in the AVL FireTM simulations, a symmetry condition is used, reducing the total number of computational cells substantially. For all simulations, a constant operation temperature of $\tilde{T}_{cell} = 343.15\text{K}$ and co-flow mode, i.e. both, cathode and anode channel flow in positive x_1 -direction, is used. The boundary conditions are shown

Parameter, [unit]	Symbol	Value
Inlet mean velocity, [m s^{-1}]		
cathode	$\tilde{u}_{1,\text{in}}$	4.5
anode	$\tilde{u}_{1,\text{in}}$	4.5
Inlet gas mole fraction, [-]		
O ₂ cathode	y_{O_2}	0.21
N ₂ cathode	y_{N_2}	0.79
H ₂ anode	y_{H_2}	0.996
N ₂ anode	y_{N_2}	0.004
Relative humidity at the inlet, [%]		
operating point RH20/20		
cathode/anode	RH	20/20
operating point RH50/40		
cathode/anode	RH	50/40
operating point RH80/80		
cathode/anode	RH	80/80
Outlet pressure, [Pa]		
cathode	\tilde{p}_{amb}	101325
anode	\tilde{p}_{amb}	101325
Cell potential, [V]	\tilde{E}_{cell}	0.5 ÷ 1.2

Table 4.1: PEMFC boundary conditions for both AVL FireTM and LIT model simulations.

in Table 4.1, geometry data and material properties are listed in Table 4.3.

A benchmark polarisation curve is established with AVL FireTM simulations, red curve RH50/40 in Fig. 4.2, by altering the cell potential from 1.2V to 0.5V with a constant relative humidity RH of 50% and 40% at the cathode and anode inlet, respectively. The fitting parameters presented in Sec. 2.4 are modified manually to adjust the result obtained by the LIT model with respect to the benchmark polarisation curve.

To evaluate the LIT models' predictive capabilities, polarisation curves with a relative humidity of 20% and 80% at both channel inlets, represented by RH20/20 and RH80/80 in Fig. 4.2, respectively, are computed keeping all fitting parameters unchanged. For a high inlet relative humidity the polarisation curve qualitatively and quantitatively agrees with the 3D simulations, and deviations are of the same order of magnitude as the error between the fitted and the benchmark curve (RH50/40). For lower inlet relative

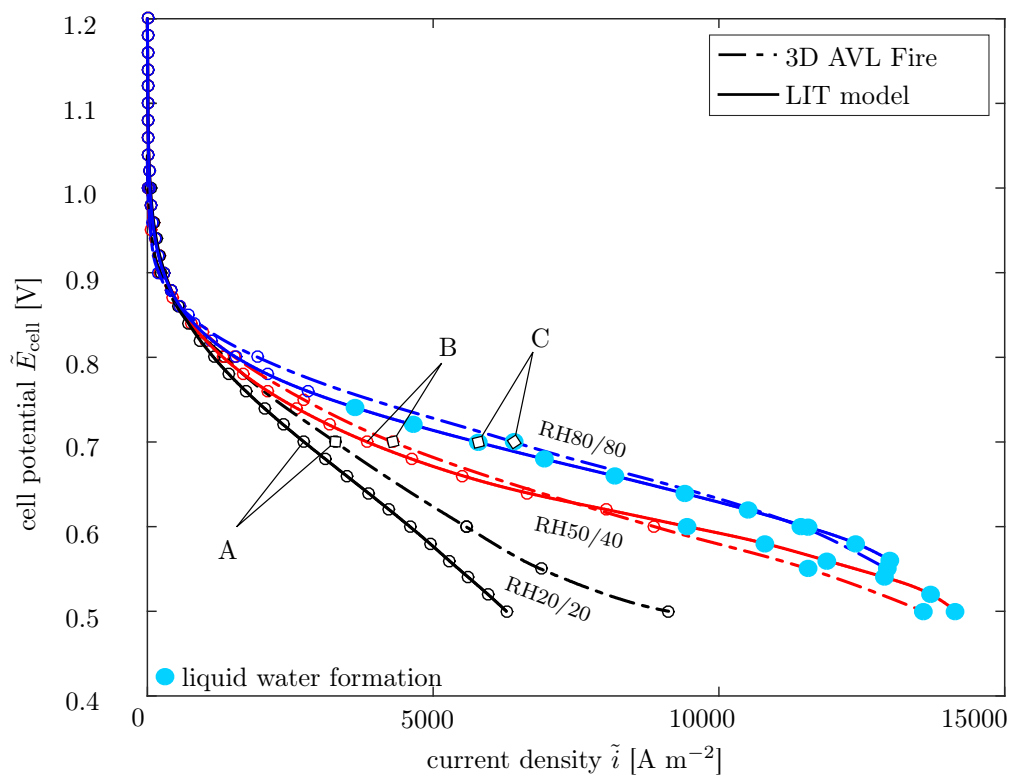


Figure 4.2: Polarisation curves simulated in AVL FireTM and the LIT model. The red lines represent the fitted benchmark case, the black and the blue lines represent the LIT model's predictive capability for different inlet humidification.

humidity a qualitative agreement, which could be further improved by an optimised fitting process, is obtained. Although phase changes are not considered within the LIT model, the normalised membrane water content can be used as an indicator for liquid water formation. Light blue dots in Fig. 4.2 indicate either a membrane water content $\lambda \geq 14$ in the LIT model or a liquid water volume fraction > 0 in the AVL FireTM simulation. Good agreement is also found in this regard. Thus, prediction of liquid water formation is assured by the LIT model.

To analyse the current density distribution along x_1 -direction, detailed results for selected steady-state operating points, denoted as A, B and C in Fig. 4.2, are presented in Fig. 4.3. Since all operating points are compared at equal cell potential $\tilde{E}_{\text{cell}} = 0.7\text{V}$, the current density offsets between the 3D and the LIT model for each relative humidity configuration in Fig. 4.2 obviously occur again in the detailed analyse in Fig. 4.3. However, characteristics agree in both models for different inlet humidification.

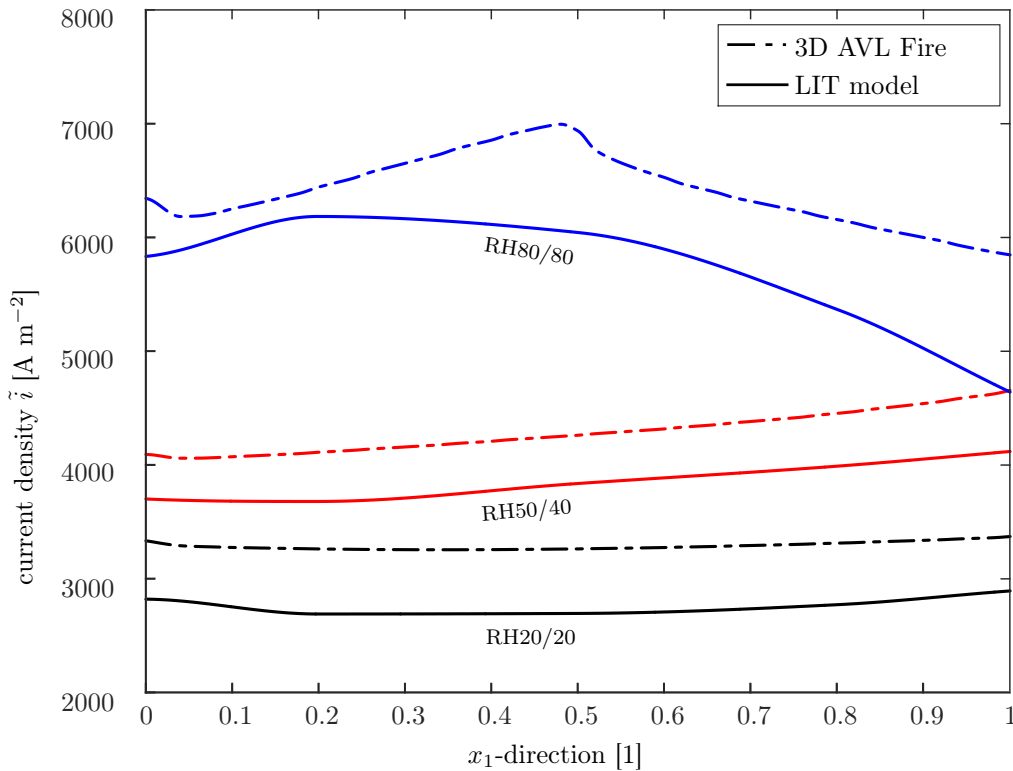


Figure 4.3: Current density distribution in x_1 -direction for selected operating points A - black, B - red and C - blue as shown in Fig. 4.2 with different relative humidity at the inlet and $\tilde{E}_{\text{cell}} = 0.7\text{V}$.

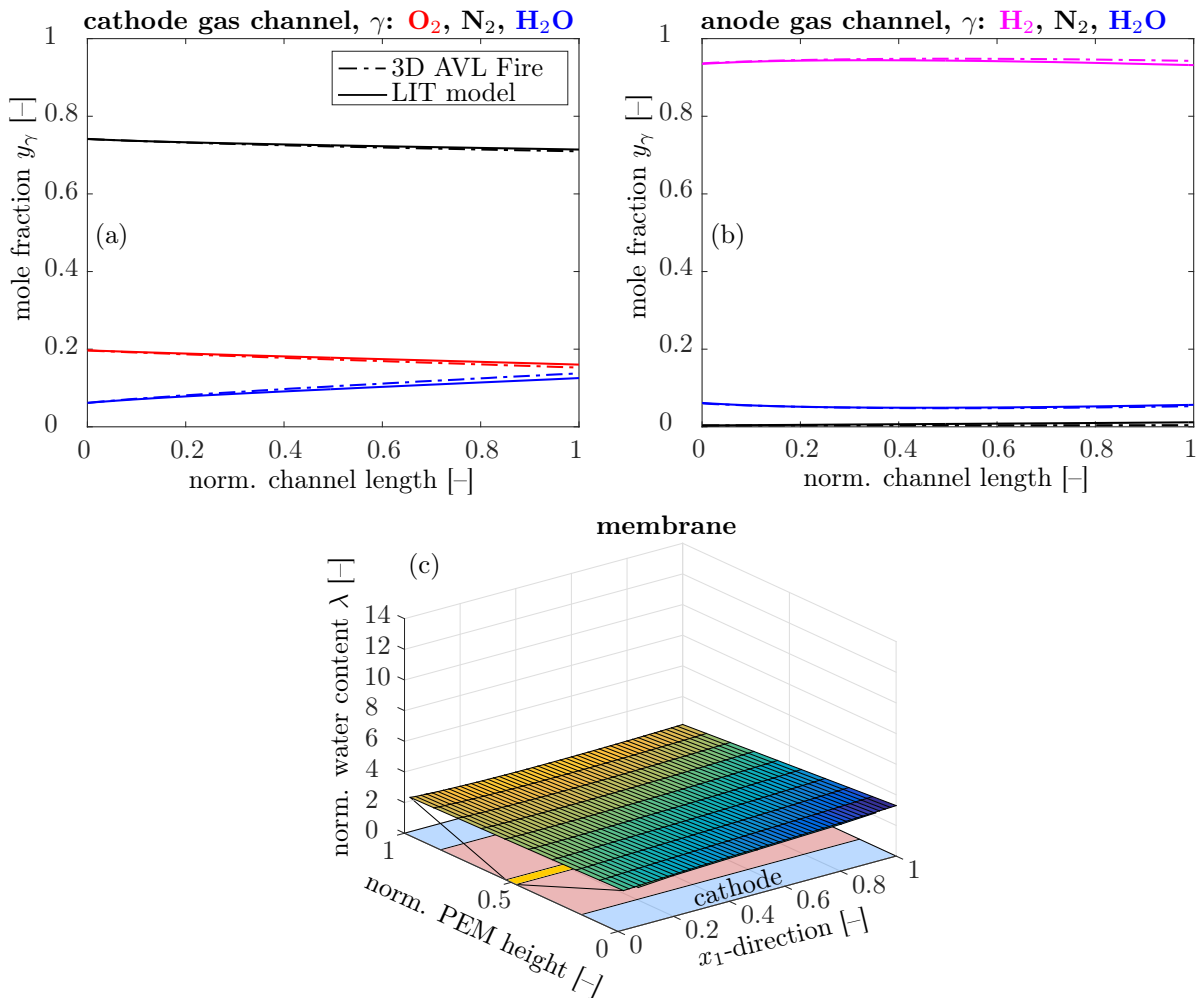


Figure 4.4: Cathode channel (a), anode channel (b) and membrane (c) species distribution for 3D AVL FireTM and the LIT model for a cell potential $\tilde{E}_{\text{cell}} = 0.7V$ and an inlet humidification of 20% at cathode and anode channel inlet. Coloured lines represent different species: red - O_2 , magenta - H_2 , black - N_2 , blue - H_2O . Fine and coarse grid for membrane water content indicates 3D AVL FireTM and LIT model, respectively.

In Figs. 4.4-4.6, the species mole fraction distribution along the cathode and the anode channels as well as the two dimensional membrane water content distribution are presented in the first, the second and the third row, respectively. Figures 4.4, 4.5 and 4.6 represent one of the three selected operating points A, B and C in Fig. 4.2, respectively. The species distributions for RH20/20 in Figs. 4.4(a,b) show remarkably good agreement with the 3D simulation results. Moreover, the accuracy is sustained at the membrane water content distribution shown in Fig. 4.4(c), where the LIT model results are slightly below the AVL FireTM simulation with an offset of $\Delta\lambda \approx 0.1$.

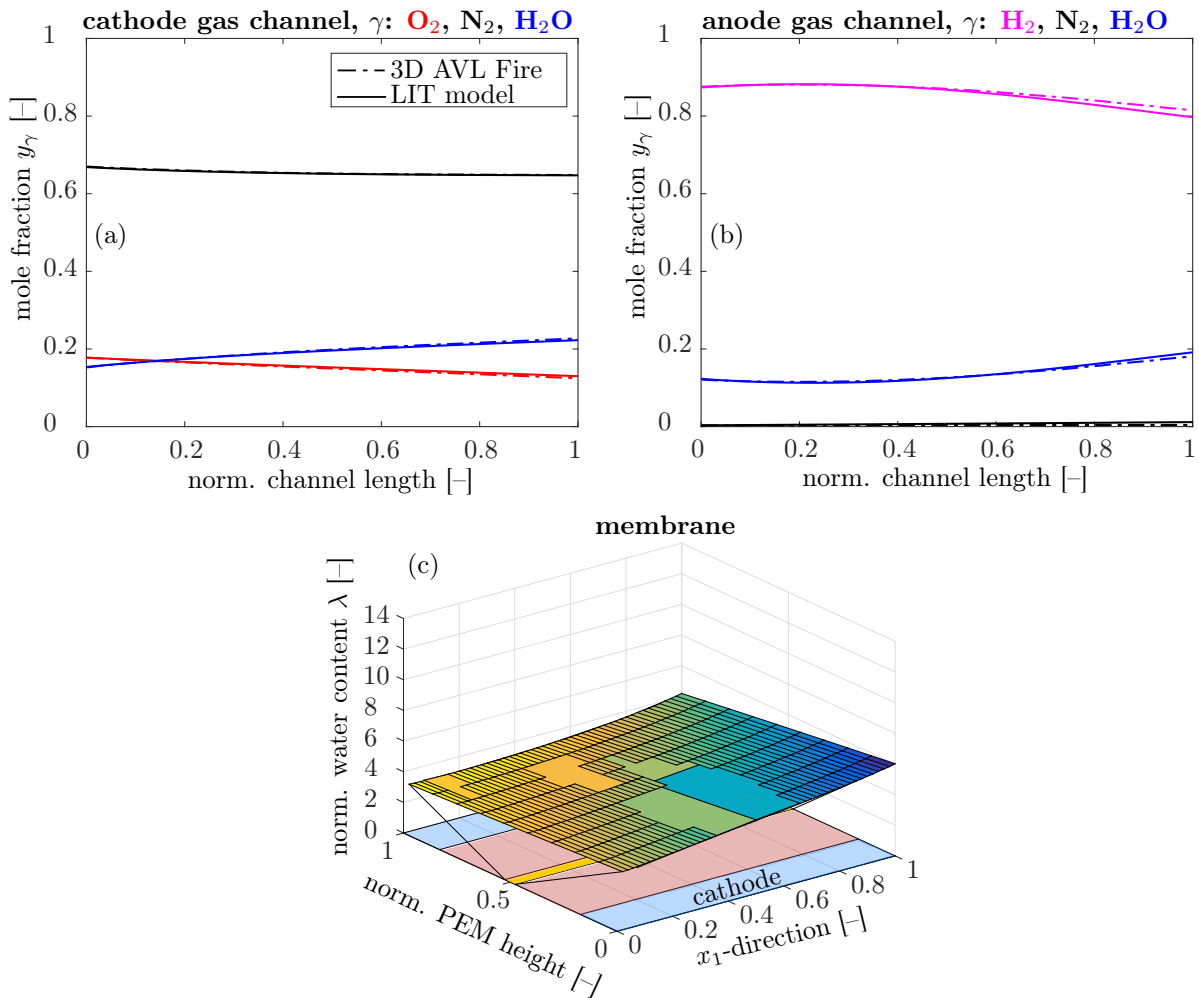


Figure 4.5: Cathode channel (a), anode channel (b) and membrane (c) species distribution for 3D AVL FireTM and the LIT model for a cell potential $\tilde{E}_{\text{cell}} = 0.7\text{V}$ and an inlet humidification of 50% and 40% at cathode and anode channel inlet, respectively. Coloured lines represent different species: red - O_2 , magenta - H_2 , black - N_2 , blue - H_2O . Fine and coarse grid for membrane water content indicates 3D AVL FireTM and LIT model, respectively.

For increased inlet humidification RH50/40 (benchmark case), the mole fraction distributions in Figs. 4.5(a,b) again match the 3D reference results. In Fig. 4.5(c), the 3D simulation and the LIT model represented by the fine and the coarse grid, respectively, coincide almost exactly. The rising gradient in x_1 -direction resulting from a higher current density and therefore increasing reaction water production can be reproduced by the LIT model, even though no x_1 dependency of λ exists due to the quasi-2D discretisation. Note that the axes are normalised with the FC's length \tilde{L} and the membrane

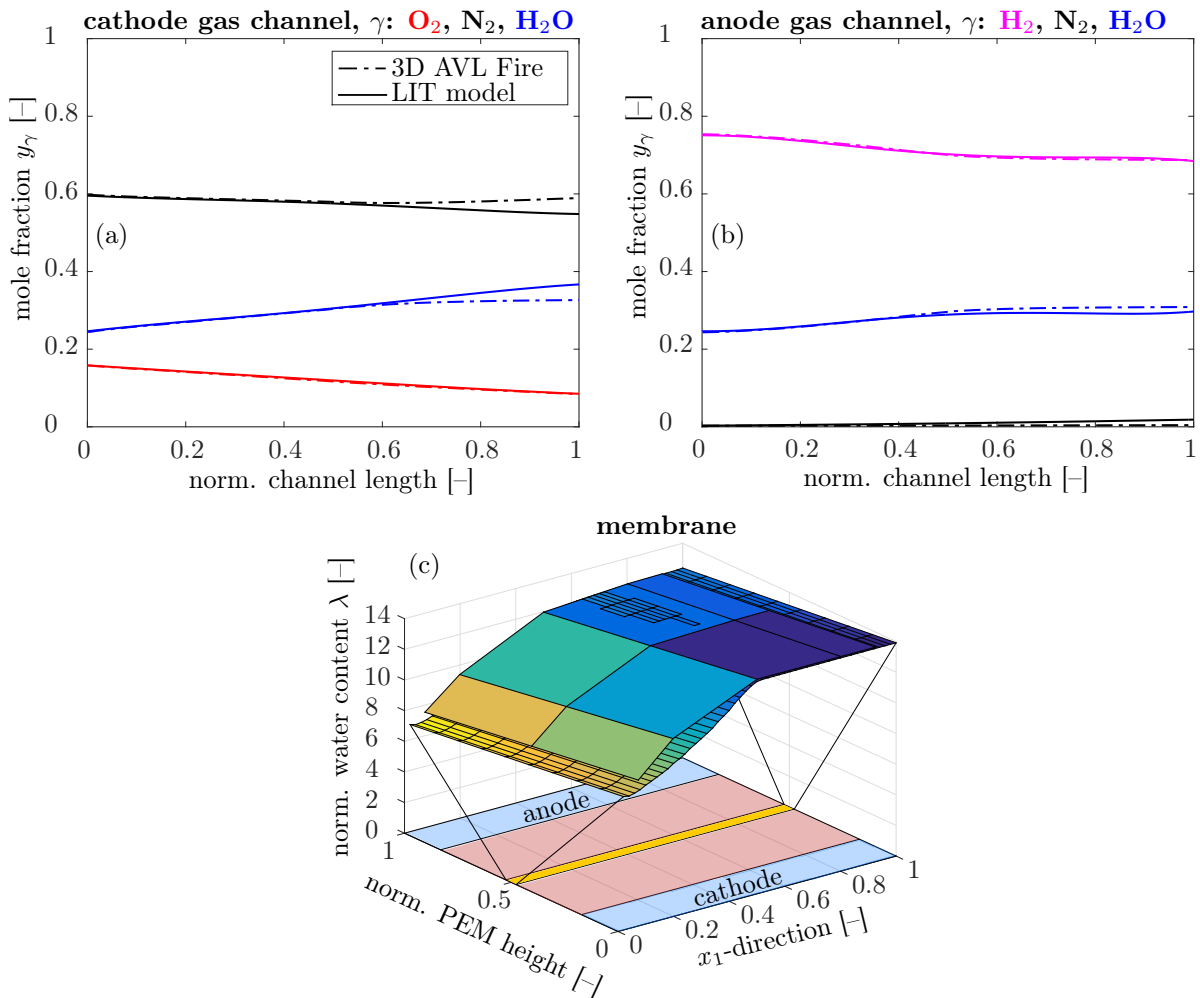


Figure 4.6: Cathode channel (a), anode channel (b) and membrane (c) species distribution for 3D AVL FireTM and the LIT model for a cell potential $\tilde{E}_{\text{cell}} = 0.7\text{V}$ and an inlet humidification of 80% at cathode and anode channel inlet. Coloured lines represent different species: red - O_2 , magenta - H_2 , black - N_2 , blue - H_2O . Fine and coarse grid for membrane water content indicates 3D AVL FireTM and LIT model, respectively.

height \tilde{H}_{PEM} in x_1 - and x_2 -direction, respectively.

For the operating point C, with the highest considered relative humidity at the inlet, RH80/80, deviations between the LIT model and the AVL FireTM simulation appear in Figs. 4.6(a,b). Here, liquid water was found over half of the FC length in the AVL FireTM simulation, also indicated by the kink in the membrane water distribution in Fig. 4.6(c). This operating condition is far beyond the LIT model capabilities, since water is assumed to be gaseous only and liquid water formation is not considered. As

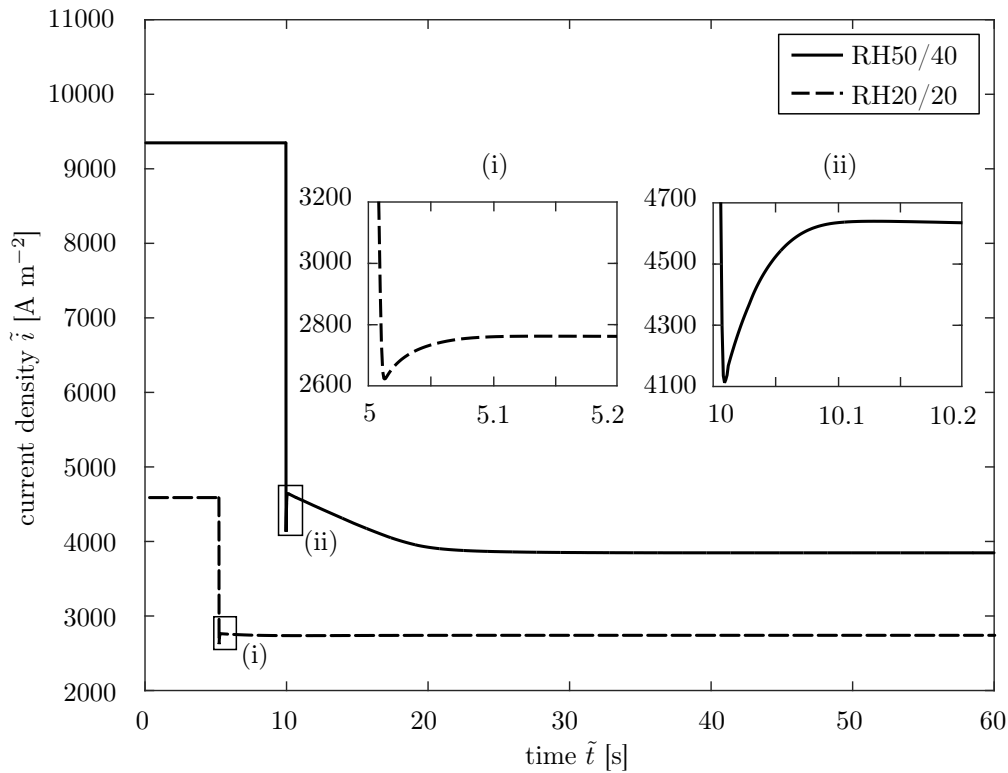


Figure 4.7: Dynamic current density response for a change of relative humidity at the inlet within 0.01s from 20% on both sides to 50% and 40% on cathode and anode side, respectively.

a consequence, the partial pressure of gaseous water $p_{\text{H}_2\text{O}}$ can exceed the saturation partial pressure p_{sat} . Whenever major deviations in the species distribution, as in Fig. 4.6(a) appear, the saturation partial pressure p_{sat} was found to be exceeded in the LIT-model results. This again reflects the accuracy of liquid water prediction in terms of membrane water content. However, at the anode side no liquid water emerges, thus the species distribution is reproduced properly in Fig. 4.6(b).

A detailed validation of transient processes is difficult, as experimental data is hardly available. Therefore, the LIT model results are analysed with respect to higher order FC models presented by Wang and Wang [9] and Wu *et al.* [34]. Therefore, four state changes are considered in Fig. 4.7 and Fig. 4.8.

In Fig. 4.7, the current density responses to increasing relative humidity at the inlet for a cell potential of $\tilde{E}_{\text{cell}} = 0.7\text{V}$ (dashed line) and $\tilde{E}_{\text{cell}} = 0.6\text{V}$ (solid line) are displayed.

Both simulations start from a steady-state with a relative humidity at both channel inlets of 20%. During the first 0.01s the relative humidity at the inlet is increased in a smooth ramp-like change to 50% and 40% on cathode and anode side, respectively. Keeping all other boundary conditions unchanged, a new steady-state is reached after approximately 20s to 40s, which is in accordance with the results of both Wang and Wu, who observed time intervals between 10s to 60s to reach steady-state conditions with their simulations. According to Wang and Wang [9], the time constant $\tilde{\tau}_m$ for membrane hydration can be estimated by

$$\tilde{\tau}_m = \frac{2\tilde{F}}{\tilde{i}} \frac{\tilde{\rho}_{\text{PEM}} \tilde{H}_{\text{PEM}} \Delta\lambda}{E\tilde{W}}. \quad (4.1)$$

For the considered Nafion type membrane [24] ($E\tilde{W} = 1.1\text{kg mol}^{-1}$, $\tilde{\rho}_{\text{PEM}} = 2024.7\text{kg m}^{-3}$) with thickness $\tilde{H}_{\text{PEM}} = 35\mu\text{m}$, $\Delta\lambda = 14$ and $\tilde{i} = 10000\text{A m}^{-2}$, $\tilde{\tau}_m$ is about 17s. This estimation is in good agreement with the times required to reach the steady-state seen in Fig. 4.7. In comparison, for a Nafion 112 membrane with $\tilde{H}_{\text{PEM}} = 51\mu\text{m}$, Wang computed a time constant $\tilde{\tau}_m = 25\text{s}$. The details (i) and (ii) in Fig. 4.7 provide a view at the short time period ($0 \div 0.2\text{s}$) after the boundary conditions are changed. Due to the increasing relative humidity at the inlet, the membrane ionic conductivity and therefore the current density is increased at the beginning of the cell, resulting in a temporal current density maximum within the first 0.05s in both simulations. As a consequence of higher humidified inlet gases, the amount of fuel gases is reduced. When these higher humidified gases reach parts of the PEM further downstream, a converse effect results in a temporarily decreasing current density until about 0.1s. However, the ongoing membrane humidification results in an increasing conductivity and the reaction current density rises on the long term scale.

In Fig. 4.8, the dynamic current density responses are displayed for a smoothly increased cell potential from $\tilde{E}_{\text{cell}} = 0.6\text{V}$ to $\tilde{E}_{\text{cell}} = 0.7\text{V}$ within 0.01s. Starting from a steady-state, these state changes are performed with a relative humidity at the channel inlet of 20% on both sides (dashed line) as well as 50% and 40% on cathode and anode side, respectively (solid line). For the sake of visualisation, the state changes are initiated at arbitrary times of 5s and 10s. The details (i) and (ii) in Fig. 4.8, show that both response curves undergo an initial undershoot followed from an overshoot, which both

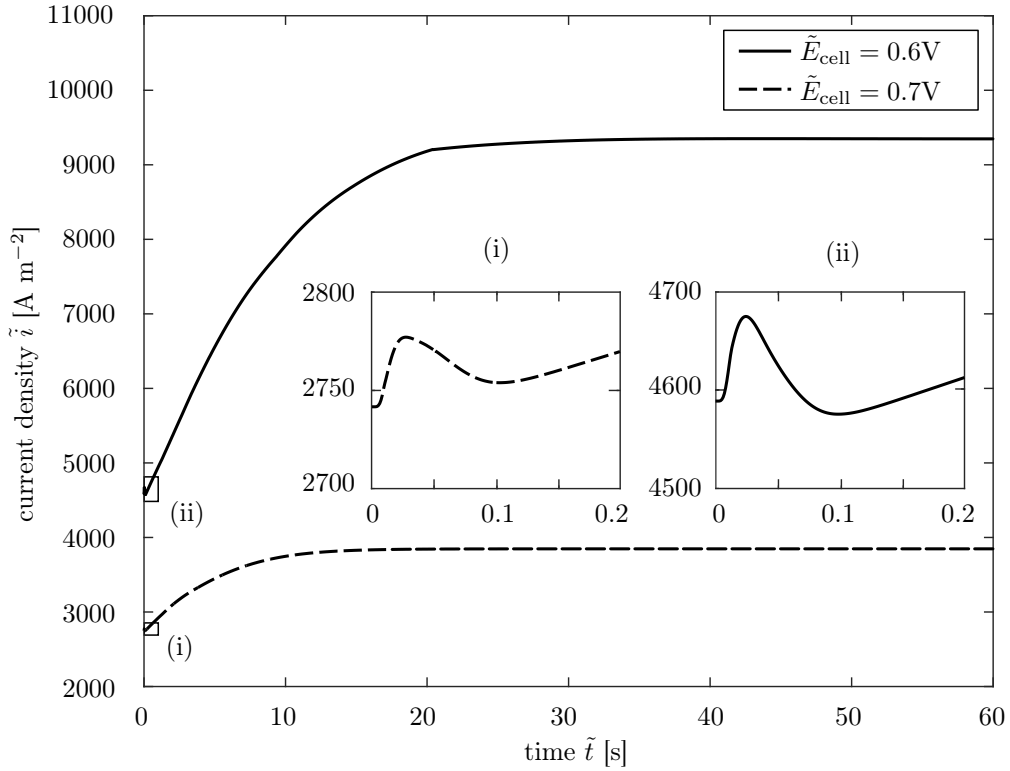


Figure 4.8: Dynamic current density response to an increasing cell potential from $\tilde{E}_{\text{cell}} = 0.6\text{V}$ to $\tilde{E}_{\text{cell}} = 0.7\text{V}$ within 0.01s.

are similarly reported by Wang and Wang [9] and Wu *et al.* [34]. The dynamics on the long term scale again show the dominance of the membrane water transport.

$N_{\text{GC}}^{\text{C,A}}$	$N_{\text{GDL}}^{\text{C,A}}$	N_{PEM}	N_{SL}	$N_A \times N_A$	S_A	t_c
8	4	3	5	356^2	0.968	44.57s
8	4	5	5	366^2	0.968	51.66s
10	4	3	5	380^2	0.966	57.17s
8	6	3	5	476^2	0.971	62.15s
8	4	3	7	460^2	0.974	75.22s

Table 4.2: Required computation time t_c for various discretisations for an inlet humidification change from RH20/20 to RH50/40 with a cell potential $\tilde{E}_{\text{cell}} = 0.7\text{V}$ presented as dashed line in Fig. 4.2(a) with a simulation time of 60s. $N_{\text{GC}}^{\text{C,A}}$, $N_{\text{GDL}}^{\text{C,A}}$, N_{PEM} and N_{SL} denote the number of nodes for the gas channel, the GDL, the membrane and the number of inner slices, respectively. The dimension and the sparsity of the square system matrix \mathbf{A} in Eq. (3.5) are indicated as $N_A \times N_A$ and S_A , respectively.

The platform, used to compute all presented LIT model results was an energy-saving Intel NUC Kit (Intel Core i5-5300U vPro 2.3GHz CPU, 8GB RAM). Although this platform is not optimised for running fast simulations, due to the applied linearisation scheme, the use of spectral methods and the quasi-2D discretisation, the computation of a single time step requires less than 25ms for the computational domain presented in Fig. 2.1(b). The implementation of variable time stepping further enhances real-time capability, i.e. during periods of strong time gradients the time step decreases to accurately resolve the state variations and vice versa during periods of little changes. For the transient simulations presented in Fig. 4.7 and Fig. 4.8 the dynamical time step adjustment leads to different computation times even though the simulation time remains equal. Whereas the simulations with an increasing relative humidity in Fig. 4.7 require 43.89s and 44.57s for a cell potential of $\tilde{E}_{\text{cell}} = 0.6\text{V}$ and $\tilde{E}_{\text{cell}} = 0.7\text{V}$, respectively, the simulations with a changing cell potential in Fig. 4.8 need 50.16s and 43.89s with a lower (RH20/20) and higher (RH50/40) inlet humidification, respectively. However, real-time capability is maintained for all these simulations. In order to give an overview how the LIT model's resolution affects the required computation time, the inlet humidification change from RH20/20 to RH50/40 with $\tilde{E}_{\text{cell}} = 0.7\text{V}$, represented by the dashed line in Fig. 4.2, is simulated with different discretisations. The computation times are listed in Table 4.2, where at each row only one domain is discretised differently with respect to the resolution used for the validation (first row). A look at the discretised quasi-2D model in Fig. 2.1(b) immediately reveals that a different number of GDL nodes $N_{\text{GDL}}^{\text{C,A}}$ or inner slices N_{SL} has the strongest influence on computation time. Even though the dimension $N_A \times N_A$ of the system matrix, defined in Eq. (3.6), increases drastically from 356^2 to 460^2 by using two more inner slices, the computation time not even doubles since the high sparsity is maintained (see Table 4.2).

Parameter, [unit]	Symbol	Value
PEMFC temperature, [K]	\tilde{T}_{cell}	343.15
PEMFC length, [m]	\tilde{L}	0.12
<i>Channel</i>		
anode		
height, [m]	\tilde{H}_{GC}	0.25×10^{-3}
width, [m]	\tilde{W}_{GC}	0.5×10^{-3}
cathode		
height, [m]	\tilde{H}_{GC}	0.25×10^{-3}
width, [m]	\tilde{W}_{GC}	1×10^{-3}
<i>GDL cathode and anode</i>		
height, [m]	\tilde{H}_{GDL}	3×10^{-3}
width, [m]	\tilde{W}_{GDL}	1.5×10^{-3}
porosity, [-]	ε	0.78
Bruggeman exponent, [-]	q	1.5
hydraulic permeability, [m ²]	$\tilde{\kappa}$	1.07×10^{-14}
<i>Catalyst layer</i>		
electrode roughness, [-]	$\tilde{a}_c \tilde{L}_c$	500
activation energy for O ₂ reduction on Pt, [J mol ⁻¹]	\tilde{E}_{act}	66×10^3
reference exchange current density, [A m ⁻²]	$\tilde{i}_{0,r}$	0.2×10^{-3}
open circuit potential, [V]	\tilde{E}_{OC}	1.229
reference O ₂ partial pressure, [Pa]	$\tilde{p}_{\text{O}_2,r}$	101250
reference temperature for \tilde{i}_0 , [K]	$\tilde{T}_{0,r}$	298.15
pressure dependency coefficient, [-]	γ_c	1
<i>Membrane</i>		
thickness, [m]	\tilde{H}_{PEM}	3.5×10^{-6}
membrane density, [kg m ⁻³]	$\tilde{\rho}_{\text{PEM}}$	2024.7
equivalent weight, [kg mol ⁻¹]	$\tilde{E}\tilde{W}$	1.1
N ₂ permeance at $\tilde{T} = 343.15\text{K}$, [10 ⁹ × mol(s m Pa) ⁻¹]		
LIT model	\tilde{k}_{N_2}	$251.7 + 37.3\lambda$
AVL Fire TM	$\tilde{k}_{\text{N}_2,\text{F}}$	5.0321
water diffusion coefficient at $\tilde{T} = 343.15\text{K}$, [m ² s ⁻¹]	\tilde{D}_w	$8.9277\lambda \times 10^{-11}$
electro-osmotic drag coefficient at $\tilde{T} = 343.15\text{K}$, [-]	C_{drag}	0.1578λ
ionic conductivity fitting parameter, [-]	$f_1; f_2$	1; 0.8

Table 4.3: Geometrical dimensions and material properties of the simulation.

Chapter 5

Conclusion and outlook ^{DK}

A dynamical PEMFC model for real-time applications, addressing essential physical phenomena and nonlinear effects within a quasi-2D description, was proposed. Spectral methods, providing high accuracy with little computation nodes, are used for the discretisation of the spatial domains. Based on the continuous solution in terms of a Chebyshev polynomial, an integral coupling method for gas channel and GDL was formulated, allowing to choose the number of inner slices independently from the channel nodes. Moreover, to achieve real-time capability, a linearisation scheme was introduced, which enables a non-iterative solution method for the coupled nonlinear governing equations and operates with the same truncation error $\mathcal{O}(\Delta t^2)$ as the approximated time derivative. The model was validated in detail against 3D simulations performed with the commercial CFD package AVL FireTM. Steady-state solutions for various inlet humidification agreed excellently in terms of species and current density distributions as well as polarisation curve prediction. Even though water phase transition is not considered in this work, the model was found to be capable of accurate liquid water prediction. In dynamical simulations the model was able to capture the same effects, e.g. time constants for membrane hydration and current density undershoots by increasing relative humidity at the inlet, as other authors [10, 34] found with higher resolving 3D simulations. Furthermore, for all presented results, real-time capability was encountered, even though the simulations were performed on an energy saving Intel NUC Kit (Intel Core i5-5300U vPro 2.3GHz CPU, 8GB RAM). Next to widespread dynamical parameter studies the model may also be used as a state observer in online control units.

In a future investigation, we aim at including temperature distribution and its inherent effects on the cell performance, e.g. by considering the conservation of energy with liquid water formation.

Acknowledgement

Financial support provided by the Christian Doppler Laboratory for innovative control and monitoring of powertrain systems together with AVL List GmbH is gratefully acknowledged.

Nomenclature

Generally, superscript tilde denotes dimensional quantities.

Latin letters

\tilde{A}	cross-sectional area, [m ²]
$\tilde{a}_c \tilde{L}_c$	electrode roughness, meaning catalyst surface area per electrode geometric area, [-]
a_w	water vapour activity, [-]
C_{drag}	electro-osmotic drag coefficient in the membrane, [-]
\tilde{D}	binary diffusion coefficient, [m ² s]
\tilde{D}_H	hydraulic diameter, [m]
\tilde{D}_w	water diffusion coefficient in the membrane, [m ² s ⁻¹]
\tilde{E}_{act}	activation energy for O ₂ reduction on platinum, [J mol ⁻¹]
\tilde{E}_{cell}	cell potential, [V]
\tilde{E}_{OC}	open-circuit potential, [V]
$\tilde{E}\tilde{W}$	equivalent weight of the dry membrane, [kg mol ⁻¹]
\tilde{F}	Faraday constant, 96485.3365 C mol ⁻¹
$f_{1,2}$	fitting parameters for PEM ionic conductivity, [-]
F_c	hydraulic diameter correction factor, [-]
f_D	Darcy-Weisbach friction factor, [-]
\tilde{H}	height of channel, GDL, membrane, [m]
\tilde{i}	reaction current density, [A m ⁻²]
\tilde{i}_0	exchange current density, [A m ⁻²]

\tilde{j}	diffusive species flux, [$\text{kg m}^{-2} \text{s}^{-1}$]
\tilde{j}^{tot}	total species flux, [$\text{kg m}^{-2} \text{s}^{-1}$]
K_{1-6}	dimensionless group, [-]
$K_{e,p}$	dimensionless group, [-]
\tilde{k}_{N_2}	nitrogen permeance in the PEM, [mol (s m Pa)^{-1}]
\tilde{L}	PEMFC length, [m]
\tilde{M}	molar mass, [kg mol^{-1}]
\tilde{p}	pressure, [Pa]
\tilde{p}_{amb}	ambient pressure, [Pa]
\tilde{p}^{sat}	saturation pressure, [Pa]
q	Bruggeman exponent, [-]
\tilde{R}	universal gas constant, $8.314 \text{ J (mol K)}^{-1}$
RH	relative humidity at channel inlet, [-]
$S_{m,u,s}$	source terms for conservation of mass, momentum and species, respectively
\tilde{T}	temperature, [K]
\tilde{T}_{cell}	cell temperature, [K]
\tilde{t}	time, [s]
$\Delta\tilde{t}$	time step, [s]
\tilde{u}	velocity, [m s^{-1}]
\tilde{u}_{in}	inlet velocity, [m s^{-1}]
\tilde{u}_{α}	species velocity, [m s^{-1}]
\tilde{W}	width of channel, GDL, membrane, [m]

Greek symbols

α_c	catalyst layer transfer coefficient, [-]
ε	gas phase volume fraction in porous media, [-]
γ_c	pressure dependency factor for electrochemical reaction, [-]
$\tilde{\gamma}_w$	membrane water transport coefficient, [$\text{mol m}^{-2} \text{s}^{-1}$]

$\tilde{\kappa}$	hydraulic permeability, [m ²]
λ	normalised membrane water content, [-]
λ_{act}	actual normalised membrane water content in non-equilibrium model, [-]
$\tilde{\mu}$	dynamic viscosity, [Pa s]
$\tilde{\rho}$	density, [kg m ⁻³]
$\tilde{\sigma}$	membrane ionic conductivity, [S m ⁻¹]
$\tilde{\tau}_w$	wall shear stress, [N m ⁻²]
ξ	mass fraction, [-]

Subscripts and superscripts

A	anode
C	cathode
r	reference value

Abbreviations

CFD	computational fluid dynamics
FC	fuel cell
GC	gas channel
GDL	gas diffusion layer
H ₂	hydrogen
H ₂ O	water
LIT	linearisation in time
N ₂	nitrogen
O ₂	oxygen
PDE	partial differential equation
PEM	proton exchange membrane
PEMFC	proton exchange membrane fuel cell
SL	slice

Bibliography

- [1] D.M. Bernardi, M.W. Verbrugge, A Mathematical Model of the Solid-Polymer-Electrolyte Fuel Cell, *J. Electrochem. Soc.* 139 (9) (1992) 2477–2491.
- [2] T.E. Springer, T.A. Zawodzinski, S. Gottesfeld, Polymer Electrolyte Fuel Cell Model, *J. Electrochem. Soc.* 138 (8) (1991) 2334–2342.
- [3] K. Dannenberg, P. Ekdunge, G. Lindbergh, Mathematical model of the PEMFC, *J. Appl. Electrochem.* 30 (2000) 1377–1387.
- [4] P. Berg, K. Promislow, J.S. Pierre, J. Stumper, B. Wetton, Water Management in PEM Fuel Cells, *J. Electrochem. Soc.* 151 (3) (2004) A341–A353.
- [5] S.A. Freunberger, M. Santis, I.A. Schneider, A. Wokaun, F.N. Büchi, In-Plane Effects in Large-Scale PEMFCs Model Formulation and Validation, *J. Electrochem. Soc.* 153 (2) (2006) A396–A405.
- [6] A.A. Kulikovskiy, Semi-analytical 1D + 1D model of a polymer electrolyte fuel cell, *Electrochem. Commun.* 6 (2004) 696–977.
- [7] H. Wu, P. Berg, X. Li, Numerical analysis of dynamic processes in fully humidified PEM fuel cells, *Int. J. Hydrogen Energy* 32 (2007) 2022–2031.
- [8] H. Wu, X. Li, P. Berg, On the modeling of water transport in polymer electrolyte membrane fuel cells, *Electrochim. Acta* 54 (2009) 6913–6927.

- [9] Y. Wang, C.Y Wang, Transient analysis of polymer electrolyte fuel cells, *Electrochim. Acta* 50 (6) (2005) 1307–1315.
- [10] Y. Wang, C.Y Wang, Dynamics of polymer electrolyte fuel cells undergoing load changes, *Electrochim. Acta* 51 (2006) 3924–3933.
- [11] P.R. Pathapati, X. Xue, J. Tang, A new dynamic model for predicting transient phenomena in a PEM fuel cell system, *Renewable Energy* 30 (2005) 1–22.
- [12] F. Gao, B. Blunier, A. Miraoui, A. El Moudni, A Multiphysic Dynamic 1-D Model of a Proton-Exchange-Membrane Fuel-Cell Stack for Real-Time Simulation, *IEEE Trans. Ind. Electron.* 57 (6) (2010) 1853–1864.
- [13] P. Massonnat, F. Gao, R. Roche, D. Paire, D. Bouquain, A. Miraoui, Multiphysical, multidimensional real-time PEM fuel cell modeling for embedded applications, *Energy Convers. Manage.* 88 (2014) 554–564.
- [14] AVL List GmbH Manual AVL FIRE version 2014, AVL Fire (2014).
- [15] J. Spurk, N. Aksel, *Fluid Mechanics*, 2nd Edition, Springer, Berlin Heidelberg, 2008.
- [16] A.A. Hill, B. Straughan, Poiseuille flow in a fluid overlying a highly porous material, *Adv. Water Resour.* 32 (11) (2009) 1609–1614.
- [17] H. Herwig, *Strömungsmechanik - Einführung in die Physik von technischen Strömungen*, 2nd Edition, Springer, Wiesbaden, 2016.
- [18] C.R. Wilke, A Viscosity Equation for Gas Mixtures, *J. Chem. Phys* 18 (4) (1950) 517–519.
- [19] E.L. Cussler, *Diffusion: mass transfer in fluid systems*, 3rd Edition, Cambridge Univ. Press, 2009.
- [20] C. Fink, Modelling and simulation of multiphase transport phenomena in porous media with application to PEM fuel cells, Ph.D. thesis, Graz University of Tech-

nology (August 2009).

- [21] E. Fuller, P. Schettler, J. Giddings, New method for prediction of binary gas-phase diffusion coefficients, *Ind. Eng. Chem.* 58 (5) (1966) 18–27.
- [22] F. Barbir, *PEM fuel cells*, 2nd Edition, Elsevier Inc., 2013.
- [23] M. Mulder, *Basic Principles of Membrane Technology*, 2nd Edition, Kluwer Academic Publishers, 1996.
- [24] L. Karpenko-Jereb, P. Innerwinkler, A.-M. Kelterer, C. Sternig, C. Fink, P. Prenninger, R. Tatschl, A novel membrane transport model for polymer electrolyte fuel cell simulations, *Int. J. Hydrogen Energy* 39 (2014) 7077–7088.
- [25] A. Rabbani, M. Rokni, Effect of nitrogen crossover on purging strategy in PEM fuel cell systems, *Appl. Energy* 11 (2013) 1061–1070.
- [26] R.K. Ahluwalia, X. Wang, Buildup of nitrogen in direct hydrogen polymer-electrolyte fuel cell stacks, *J. Power Sources* 171 (2007) 63–71.
- [27] A.A. Kulikovskiy, *Analytical Modelling of Fuel Cells*, Elsevier, Amsterdam, 2010.
- [28] The Mathworks, Inc., Natick, Massachusetts, United States, *MATLAB Release 2015a* (2015).
- [29] L.N. Trefethen, *Spectral Methods in Matlab*, SIAM, Philadelphia, 2000.
- [30] L.N. Trefethen et al., *Chebfun version 5.3.0* (2015).
URL <http://www.chebfun.org>
- [31] S. Scheichl, S. Braun, A. Kluwick, On a similarity solution in the theory of unsteady marginal separation, *Acta Mech.* 201 (2008) 153–170.
- [32] T.W.H. Sheu, R.K. Lin, Newton linearization of the incompressible Navier-Stokes equations, *Int. J. Numer. Meth. Fluids* 44 (2004) 297–321.

- [33] J.P. Berrut, L.N. Trefethen, Barycentric Lagrange Interpolation, *SIAM Rev.* 46 (3) (2004) 501–517.
- [34] H. Wu, P. Berg, X. Li, Non-isothermal transient modeling of water transport in PEM fuel cells, *J. Power Sources* 165 (2007) 232–243.
- [35] Verein Deutscher Ingenieure, VDI Heat Atlas, 2nd Edition, Springer Berlin Heidelberg, Berlin, Heidelberg, 2010.
- [36] National Institute of Standards and Technology, NIST Chemistry WebBook, accessed: 2017-05-09.
URL <http://webbook.nist.gov/chemistry/fluid/>
- [37] L. Greengard, Spectral integration and two-point boundary value problems, *SIAM J. Numer. Anal.* 28 (4) (1991) 1071–1080.

Appendix A

Dimensionless groups ^{DM}

To obtain the non-dimensional form of the governing equations, consequently each variable is replaced by a dimensionless variable multiplied with a characteristic reference value. For an arbitrary variable \tilde{s} this reads:

$$\tilde{s} = \tilde{s}_r s,$$

where \tilde{s} , \tilde{s}_r and s denote a dimensional, characteristic and dimensionless variable, respectively. Characteristic values for each variable and domain are listed in Table A.1.

Hence, the dimensionless groups appearing in Table 2.1 and Eq. (2.15) read:

$$\begin{aligned} K_1^{C,A} &= \frac{\tilde{L}_1}{\tilde{H}_{GC}} \frac{\tilde{W}_{GDL}}{\tilde{W}_{GC}} \frac{1}{Pe}, & K_2^{C,A} &= \frac{\tilde{L}_1}{\tilde{H}_{GC}} \frac{\tilde{W}_{GDL}}{\tilde{W}_{GC}} \frac{8}{Re}, \\ K_3^{C,A} &= K_1^{C,A}, & K_4^{C,A} &= Sc, \\ K_5^{C,A} &= \frac{\tilde{L}_2^2}{\tilde{\kappa}} Sc, & K_6 &= \frac{E\tilde{W}}{\tilde{\rho}_{PEM}} \frac{\tilde{i}_r}{\tilde{H}_{PEM}} \frac{\tilde{t}_{PEM,r}}{F} C_{drag}. \end{aligned}$$

Dimensionless groups appearing in Eqs. (2.10) and (2.13) read:

$$K_{p,1} = \frac{1}{F_c}, \quad K_{p,2} = 1, \quad K_{e,a}^{C,A} = \frac{\tilde{R}}{\tilde{U}_a^2} \frac{\tilde{T}_r}{\tilde{\mathcal{M}}_r}.$$

$(\tilde{\cdot})_r$	channel, $a = 1$		GDL, $a = 2$		PEM
	cathode	anode	cathode	anode	
E_{cell}	–	–	–	–	E_{OC}
i	–	–	–	–	i_r
p	$\rho_{\text{air}} u_{1,\text{in}}^2$	$\rho_{\text{H}_2} u_{1,\text{in}}^2$	$\rho_{\text{air}} \frac{\mathcal{D}_{\text{O}_2,\text{H}_2\text{O}}^2}{H_{\text{GDL}}^2}$	$\rho_{\text{H}_2} \frac{\mathcal{D}_{\text{H}_2,\text{H}_2\text{O}}^2}{H_{\text{GDL}}^2}$	–
T	T_{cell}	T_{cell}	T_{cell}	T_{cell}	T_{cell}
t	$\frac{L}{u_{1,\text{in}}}$	$\frac{L}{u_{1,\text{in}}}$	$\frac{H_{\text{GDL}}^2}{\mathcal{D}_{\text{O}_2,\text{H}_2\text{O}}}$	$\frac{H_{\text{GDL}}^2}{\mathcal{D}_{\text{H}_2,\text{H}_2\text{O}}}$	$\frac{H_{\text{PEM}}^2}{D_w}$
u	$u_{1,\text{in}}$	$u_{1,\text{in}}$	$\frac{H_{\text{GDL}}}{\mathcal{D}_{\text{O}_2,\text{H}_2\text{O}}}$	$\frac{H_{\text{GDL}}}{\mathcal{D}_{\text{H}_2,\text{H}_2\text{O}}}$	–
L	L	L	H_{GDL}	H_{GDL}	H_{PEM}
\mathcal{D}	–	–	$\mathcal{D}_{\text{O}_2,\text{H}_2\text{O}}$	$\mathcal{D}_{\text{H}_2,\text{H}_2\text{O}}$	D_w
\mathcal{M}	\mathcal{M}_{O_2}	\mathcal{M}_{H_2}	\mathcal{M}_{O_2}	\mathcal{M}_{H_2}	–
μ	μ_{air}	μ_{H_2}	μ_{air}	μ_{H_2}	–
ρ	ρ_{air}	ρ_{H_2}	ρ_{air}	ρ_{H_2}	ρ_{PEM}

Table A.1: Characteristic values used to obtain the dimensionless formulation of the governing equations. Since all entries in this table are dimensional values, tilde is omitted for simplicity.

Commonly used dimensionless groups such as the Reynolds number Re , the Schmidt number Sc and the Peclet number Pe appearing in the coefficients above are defined for cathode and anode as follows. Their numerical values are computed, with reference values used for the validation (see Tables 4.1, 4.3 and A.2).

$$\begin{aligned} \text{cathode: } \text{Re} &= \frac{\tilde{u}_{1,\text{in}} \tilde{D}_{\text{H}} \tilde{\rho}_{\text{air}}}{\tilde{\mu}_{\text{air}}} = 88.86, \\ \text{Sc} &= \frac{\tilde{\mu}_{\text{air}}}{\tilde{\mathcal{D}}_{\text{O}_2,\text{H}_2\text{O}} \tilde{\rho}_{\text{air}}} = 0.6, \\ \text{Pe} &= \frac{\tilde{u}_{1,\text{in}} \tilde{H}_{\text{GDL}}}{\tilde{\mathcal{D}}_{\text{O}_2,\text{H}_2\text{O}}} = 39.96, \end{aligned}$$

$$\begin{aligned} \text{anode: } \text{Re} &= \frac{\tilde{u}_{1,\text{in}} \tilde{D}_{\text{H}} \tilde{\rho}_{\text{H}_2}}{\tilde{\mu}_{\text{H}_2}} = 10.79, \\ \text{Sc} &= \frac{\tilde{\mu}_{\text{H}_2}}{\tilde{D}_{\text{H}_2,\text{H}_2\text{O}} \tilde{\rho}_{\text{H}_2}} = 1.24, \\ \text{Pe} &= \frac{\tilde{u}_{1,\text{in}} \tilde{H}_{\text{GDL}}}{\tilde{D}_{\text{H}_2,\text{H}_2\text{O}}} = 12.02. \end{aligned}$$

Parameter, reference, [unit]	Symbol	Value
molar mass O ₂ , [35], [kg mol ⁻¹]	$\tilde{\mathcal{M}}_{\text{O}_2}$	31.9988×10^{-3}
molar mass H ₂ , [35], [kg mol ⁻¹]	$\tilde{\mathcal{M}}_{\text{H}_2}$	2.016×10^{-3}
dynamic viscosity air, [35], [Pa s]	$\tilde{\mu}_{\text{air}}$	20.56×10^{-6}
dynamic viscosity H ₂ , [36], [Pa s]	$\tilde{\mu}_{\text{H}_2}$	9.813×10^{-6}
density air, [35], [kg m ⁻³]	$\tilde{\rho}_{\text{air}}$	1.015
density H ₂ , [36], [kg m ⁻³]	$\tilde{\rho}_{\text{H}_2}$	0.0706
binary diffusion coefficient, [21]		
O ₂ -H ₂ O, [m ² s ⁻¹]	$\tilde{D}_{\text{O}_2,\text{H}_2\text{O}}$	26.52×10^{-6}
H ₂ -H ₂ O, [m ² s ⁻¹]	$\tilde{D}_{\text{H}_2,\text{H}_2\text{O}}$	112.36×10^{-6}
reference current density, [A m ⁻²]	\tilde{i}_{r}	14000

Table A.2: Reference gas properties at $\tilde{T} = 343.15\text{K}$, $\tilde{p} = 10^5\text{Pa}$ and reference current density used to compute dimensionless groups.

Due to the lack of a characteristic convective velocity in the GDLs, the reference velocity $\tilde{u}_{2,\text{r}}$ is computed via the corresponding reference diffusion coefficient (see Table A.1). This and neglecting diffusion in the gas channels lead to the Schmidt number Sc and the Reynolds number Re as single dimensionless groups characterising the GDL and the gas channel, respectively. Consequently, the Peclet number $\text{Pe} = \tilde{u}_{1,\text{r}}/\tilde{u}_{2,\text{r}}$ appears as ratio of the characteristic velocities for channel and GDL, in the source terms which are coupling these domains.

Appendix B

LIT PEMFC model - user guide

The LIT PEMFC model is a real-time capable reduced order fuel cell model based on a quasi-2D discretisation [3] and the application of a linearisation with respect to the previous time step [32], solved with a Chebyshev collocation method. In the corresponding domains, the model encounters the following physical phenomena:

- The gas channels (GCs) are assumed to be convection driven only.
- In the gas diffusion layers (GDLs) convection, multicomponent diffusion described by generalised Fick's law of diffusion are assumed as driving forces. Darcy's law is considered for the pressure loss in the porous media.
- For the proton exchange membrane (PEM) water transport, electro-osmotic drag and water diffusion are considered and the membrane nitrogen (N_2) crossover is driven by a partial pressure gradient.
- For the electrochemical model, activation losses on cathode side and the membrane ohmic losses depending on the membrane water loading are considered.

The entire model is implemented in Matlab[®], [28] and structured in three different categories:

1. three input files:

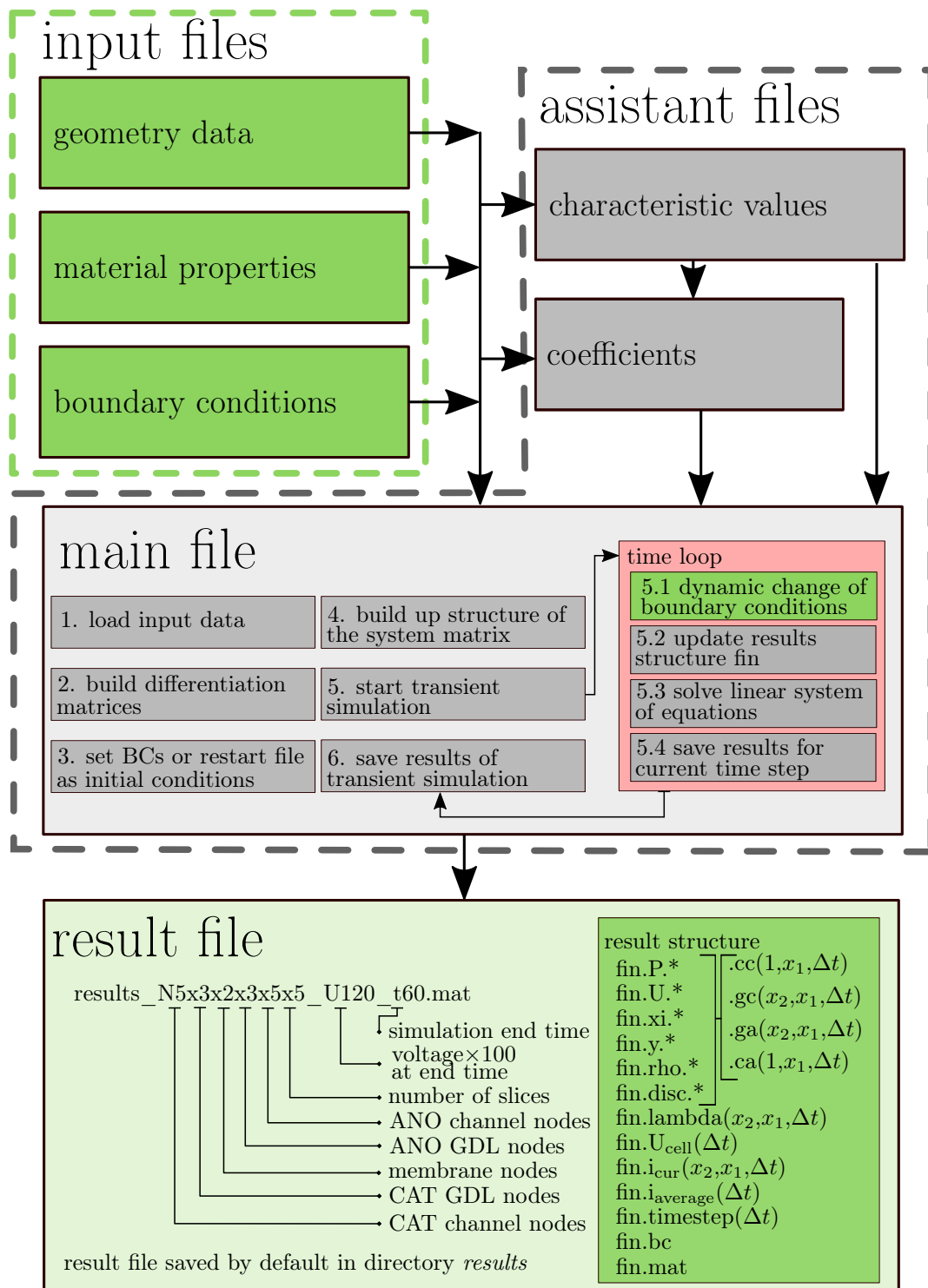


Figure B.1: LIT-Model flow diagram. Green fields denote domains for user interaction.

- Geometry.m,
 - Material.m,
 - Boundary_Conditions.m,
2. two assistant files:
- Characteristic_Values.m,
 - Coefficients.m and
3. one main file:
- Main.m.

The flow diagram in Fig. B.1 illustrates the interaction between the different files.

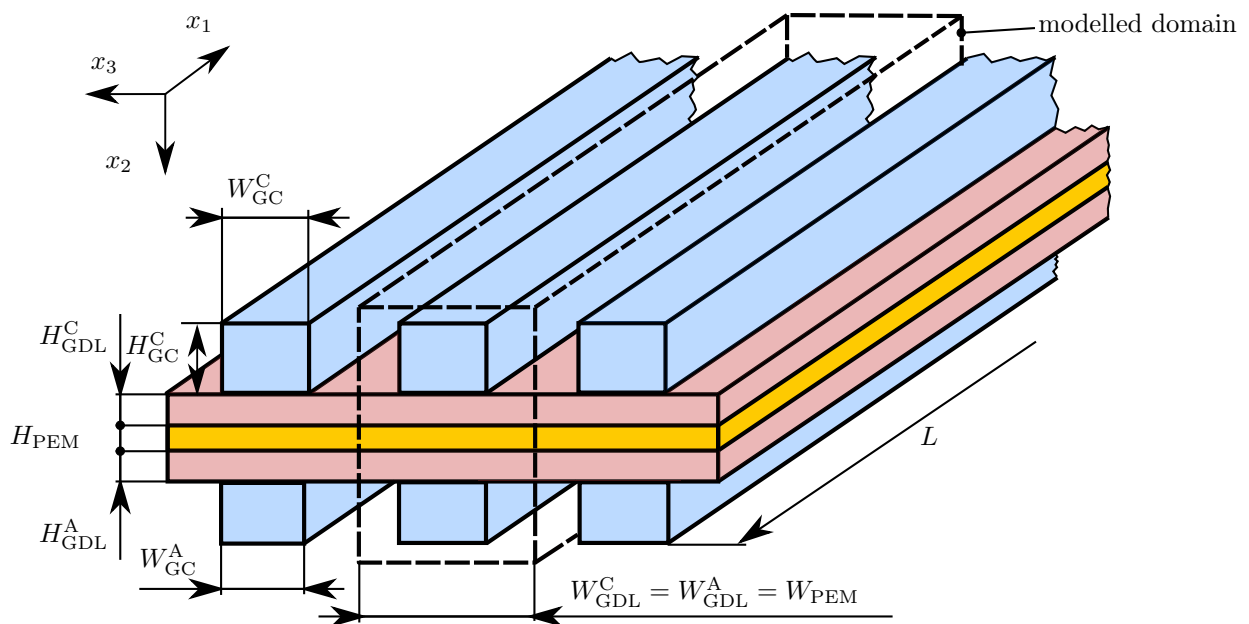


Figure B.2: Modelled domain considered in the LIT model with the corresponding dimensions. Whereas the width of anode and cathode gas channel can be different, the width of GDLs and membrane must be equal.

B.1 Input files ^{DM}

B.1.1 Geometry data

Here the proton exchange membrane fuel cell (PEMFC) geometry data for the different domains, namely:

1. the gas channel,
2. the gas diffusion layer,
3. the catalyst layer and
4. the proton exchange membrane

are defined, see Fig. B.2.

Note, whereas the length of all domains and the width of the PEM and the anode (ANO) and the cathode (CAT) GDL must be equal, the channel widths on anode and cathode side can be chosen independently, as indicated in Fig. B.2.

For further use during the computation, all values set in the file `Geometry.m` are saved in the structure `geom`.

B.1.2 Material properties

Set universal constants and material properties:

- the universal gas constant R and the Faraday constant F ,
- the feed gas molar masses, the viscosity of the present species, etc.,
- the GDL permeability and the volume fraction,

- the thickness, the water permeability and the ohmic conductivity of the PEM and
- properties for the electrochemical reaction such as the activation energy, the reference oxygen O₂ partial pressure, etc.

The desired coupling method between GDL and membrane can be selected here. The two possibilities are:

- Assuming equilibrium between GDL and membrane and hence coupling these domains via the equilibrium membrane water sorption presented by Springer *et al.* [2]. Therefore, the normalised membrane water content λ at the interface is computed by the GDL's water vapour activity a_w ,

$$\lambda = 0.043 + 17.81a_w - 39.85a_w^2 + 36.0a_w^3 . \quad (\text{B.1})$$

- Use the non-equilibrium approach of Berg *et al.* [4], which computes a flux \tilde{j}_w across the interface from the difference between equilibrium membrane water content λ and the actual non-equilibrium value λ_a , by defining a water transfer coefficient $\tilde{\gamma}_w$,

$$\tilde{j}_w = \tilde{\gamma}_w (\lambda_a - \lambda) . \quad (\text{B.2})$$

```

71 | % MEMBRANE COUPLING (equilibrium/nonequilibrium)
72 |     mem_cpl           = 'equilibrium' % Springer polynomial
73 | %     mem_cpl         = 'nonequilibrium' % gamma law
74 | % TRANSFER COEFFICIENT FOR NON-EQUILIBRIUM MEMBRANE/GDL COUPLING [Berg2004], [mol
    | / (m^2 s)]
75 |     mem.gamma.a       = 1e-2;
76 |     mem.gamma.c       = 1e-2;

```

Next to material properties, fitting parameters – allowing to calibrate the electrochemical properties, the membrane ohmic conductivity with respect to an existing set-up – can be adjusted in this file.

The following fitting parameters for the electrochemical reaction in Eqs. (2.18), (2.19) can be tuned:

- catalyst layer transfer coefficient $\tilde{\alpha}$,
- electrode roughness, meaning catalyst surface area per electrode geometric area $\tilde{a}_c \tilde{L}_c$,
- pressure dependency factor for electrochemical reaction $\tilde{\gamma}_c$ and
- reference exchange current density, $\tilde{i}_{0,r}$.

For the membrane ohmic conductivity [2], Eq. (2.20), two fitting parameters f_1, f_2 can be used:

$$\tilde{\sigma} = (-0.326f_1 + 0.5139f_2 \lambda) \exp\left(\frac{1286}{303} - \frac{1286K}{\tilde{T}}\right) \quad (\text{B.3})$$

The corresponding lines in the material file read:

```

126 % ELECTROCHEMISTRY FITTING PARAMETERS
127 % REFERENCE EXCHANGE CURRENT DENSITY [A/m^2]
128 cl.i0_ref          = 200e-6;
129 % ELECTROCATALYTIC SURFACE AREA [1/m]
130 cl.a_c            = 1000;
131 % CATALYST LOADING [mg Pt/cm^2]
132 cl.L_c           = 0.5;
133 % PRESSURE DEPENDENCY FACTOR
134 cl.gamma         = 1;
135 % TRANSFER COEFFICIENT CATALYST LAYER
136 cl.alpha         = .57;
137 % CONDUCTIVITY FITTING PARAMETER
138 con_fitB = 0.8;
139 con_fitA = 1;

```

For further use in the computation, all values entered in the file `Material.m` are saved in the structure `mat`.

B.1.3 Boundary conditions

In the file `Boundary_Condition.m`, the general simulation settings are defined:

- the inlet and outlet boundary conditions of the GCs,

- the fuel cell voltage,
- the preferred operating modes,
- the simulation time, the time step, activation of variable time stepping,
- the spatial discretisation,
- the initialisation and the start of a simulation from a restart file.

Inlet and outlet boundary conditions of the GCs

On both anode and cathode side, the feed gas compositions must be set at the gas channel inlet. Note that only two out of three mass fractions can be set, as the third one is calculated via the closure equation $\sum_{i=1}^3 x_i = 1$. Similar, the density can not be set as a boundary condition, as it is directly coupled to the pressure by the equation of state for and therefore, part of the solution. Next to the inlet mass fractions, the pressure at the channel outlet and, depending on the operating mode, either the inlet velocity or pressure is set as boundary condition, i.e. mass or pressure driven operation (see Fig. B.4).

Fuel cell potential

A constant cell potential on the bipolar plates is assumed in the electrochemical model, i.e. neglecting ohmic losses of the GDLs. By setting the cell voltage as boundary condition, the current density distribution is computed considering activation losses on the cathode side and membrane ohmic losses, see Fig. B.3.

Operating modes

The LIT model handles multiple operating modes; whereas mass or pressure driven operation is achieved by using different sets of boundary conditions, feed gas configuration

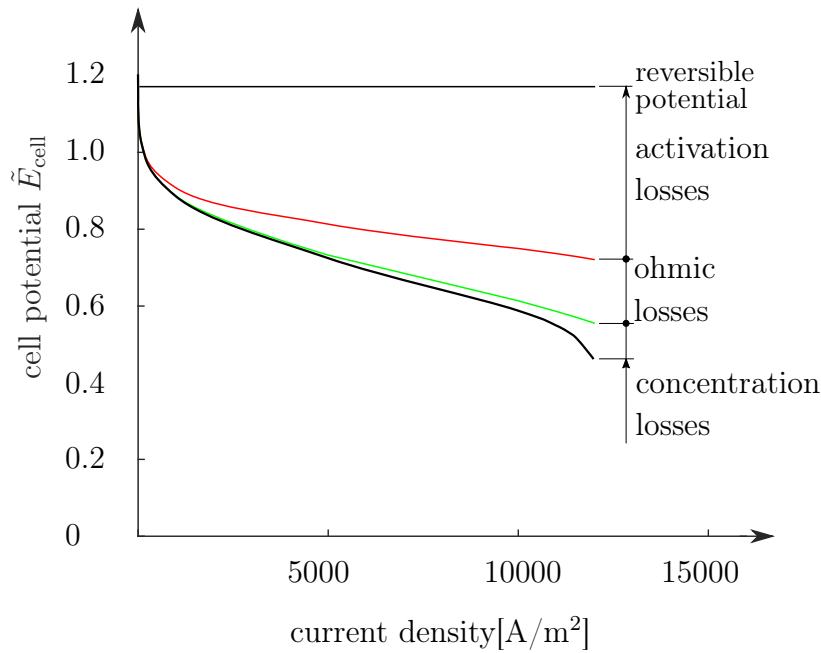


Figure B.3: Polarisation curve with activation potential, ohmic and concentration potential losses.

for co- or counter flow is realised by exchanging the anode channel boundary conditions for inlet and outlet, see Fig. B.4. In the case of counter-flow simply the anode GC flow direction is switched. To chose the desired operating mode, the corresponding lines have to be commented out. The corresponding set of boundary conditions is automatically applied at the required computational nodes.

```

28 | %% 2. INLET PROPERTIES
29 | % FLOW DIRECTION (co-flow/counter-flow)
30 |     flow = 'co'
31 | %     flow = 'counter'
32 | % MASS TRANSPORT (mass/pressure driven)
33 |     transport = 'mass'
34 | %     transport = 'pressure'

```

Variable time stepping

The time derivative is approximated by a scheme of second order in time $\mathcal{O}(\Delta t^2)$ capable of variable time stepping, see Eq. (3.2). If this is enabled, the constant time step defined in the `Boundary_Conditions.m` file serves as the initial time step and the

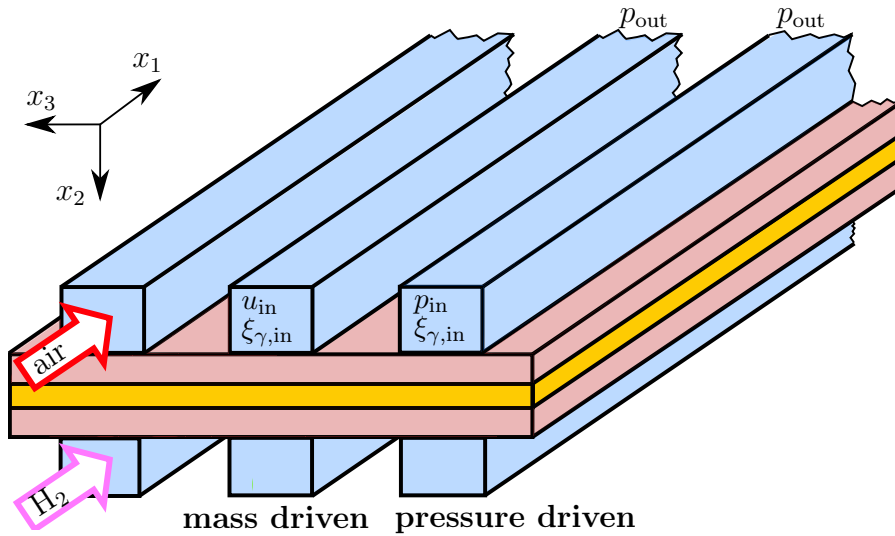


Figure B.4: Different boundary conditions are applied for mass or pressure driven simulations.

actual time step is increased or decreased linearly if the time gradients of current density or membrane water content go below or above an empirical value (`iGradLim_u`, `iGradLim_l`, `lambdaGradLim`) respectively. The time step adoption is limited to a user defined domain $[\Delta t_{\min}, \Delta t_{\max}]$. Currently, empirical values for the time gradient of the membrane water content and the current density are used as limit values for the time step adjustment. The factors `ts_increase` and `ts_decrease` are applied to increase the time step ratio α , respectively.

For these settings, the corresponding lines in the boundary conditions file read:

```

19  %% 1. TIME DISCRETISATION
20      endtime = 120;
21  % VARIABLE TIME STEP (on/off)
22      varDT   = 'on'
23  %   varDT   = 'off'
24  % VARIABLE TIME STEP (parameters for time step change, see Sec. 6. further down
25      dtLim_u = 3.5e-2; % upper limit time step
26      dtLim_l = 1e-3;  % lower limit time step
27  % CONSTANT TIME STEP
28      timestep = 1e-3;

140 %% 5. PARAMETERS FOR VARIABLE TIME STEP
141     lambdaGradLim = 1.3; % limit to decrease time step
142     iGradLim_u    = 550; % limit to decrease time step
143     iGradLim_l    = 350; % limit to increase time step
144     ts_decrease   = 0.5; % factor to decrease time step

```



```
145 | ts_increase = 1.02; % factor to increase time step
```

Spatial discretisation

As displayed in Fig. 2.1(a), the discretisation of each domain can be set independently. However, the multiple inner slices are discretised equally. The dimension N_A of the square matrix \mathbf{A} , given by Eq. (3.6) clearly shows that the number of slices N_{SL} significantly influences the dimension of \mathbf{A} and therefore the required computation time, see Table 4.2. A range of typical discretisations for each domain are given in Table B.1. The number of membrane nodes may affect simulation stability, for more details see [37].

domain	discretisation
cathode channel nodes	5 ÷ 20
anode channel nodes	5 ÷ 20
number of inner slices	4 ÷ 10
cathode GDL nodes	4 ÷ 8
anode GDL nodes	4 ÷ 8
membrane nodes	3 ÷ 5

Table B.1: Typical discretisations for all domains

Initialisation - use restart file

By default, the computational domain of the gas channels are initialised with the applied boundary conditions. Whereas the boundary conditions of the mass fractions and zero velocity are used as initial value for the GDLs, the membrane water content λ is either set to be in equilibrium with the cathode or the anode GDL's water activity a_w . Therefore the water sorption isotherm, Eq. (B.1), which for the LIT model is approximated by four lines of best fit, see Fig. 3.2, Eq. (2.23) is used. However, it is recommended to use the anode water activity to initialise the membrane water content.

To restart from a previous simulation, simply the name of the restart file must be defined, i.e. the name of the automatically saved result file. Note, the discretisation of the spatial domain must be equal to the discretisation used in the restart file. Moreover, if the state in the restart file is not a steady-state, a restart may be harsh.

The corresponding lines in the boundary conditions file read:

```
100 %% 4. INITIALISATION
101     restart_file_name = 'results_N6x4x4x4x6x5_U60_t120_RH5040.mat';
102
103
104 % INITIALISE MEMBRANE IN EQUILIBRIUM WITH GDL
105     initialise = 'ANO'; % (recommended)
106 %     initialise = 'CAT';
```

All values set in the file `Boundary_Conditions.m` are saved in the structure `bc` for further use in the computation.

B.2 Assistant files ^{DK}

B.2.1 Characteristic values

The characteristic values set in this file are used to derive the non-dimensional form of the governing equations. These values must not be changed.

B.2.2 Coefficients

Coefficients which emerge by deriving the non-dimensional form of the governing equations are defined here. These coefficients must not be changed.

B.3 Main file ^{DM}

This file is loading the input parameters, running the simulation, saving and plotting the results in the following order:

B.3.1 Load data

The input data from the files presented in Sec. B.1 and Sec. B.2 are compiled and loaded here. This ensures that all changes made in different input files are considered.

B.3.2 Assistant variables

Constant variables such as differentiation matrices, coefficient matrices for the implicit coupling method (described in Sec. 3.3) etc., required for the function `SystemMatrix.m`, see Sec. B.4.1, which builds up and solves the linear system of equations, are computed.

B.3.3 Initial conditions

The simulation is initialised as defined in the `Boundary_Conditions.m` file, see Sec. B.1.3.

B.3.4 Time loop

In the marching scheme of a transient simulation, the governing equations must be solved once at each discrete time step. The function `SystemMatrix.m` builds up and solves the linear system of equations, see Sec. B.4.1. To run a transient simulation

with dynamic boundary conditions, the time depending boundary conditions must be applied within the time loop. Therefore, the desired conditions must be changed in the structure `bc`. For, e.g. a ramp change of the cathode channel inlet velocity this reads:

```

283 while time <=bc.endtime
284 %% 5.1 CHANGE DYNAMIC BOUNDARY CONDITIONS
285 % #####begin changes#####begin changes#####begin changes#####
286 % use BC_physical for smooth BC change
287 if time > t_start && time < (t_start + t_change)
288     bc.u_in.cc = bc.u_in_old.cc + (newBC - bc.u_in_old.cc)*(t_start +
289         t_change)/time;

```

In order to change the boundary conditions in a physically smooth manner, the function `bc_physical.m` can be used, see Sec. B.4.4.

B.3.5 Save results

If the simulation end time (set in the `Boundary_Conditions.m` file) is reached, the result structure `fin` is saved inside the folder `results` with the labelling displayed in Fig. B.1. The indices of the result structure `fin` can easily be identified in Fig. B.5.

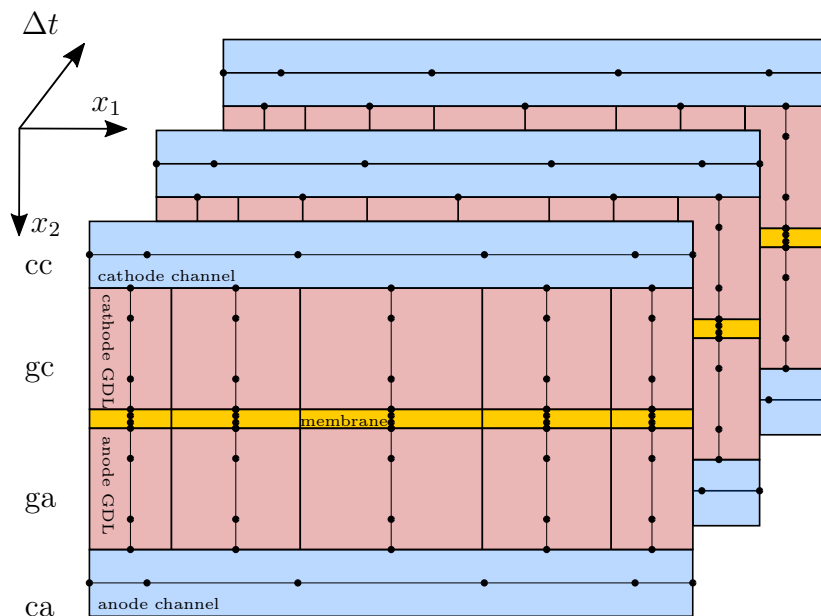


Figure B.5: Illustration of the dimension and structure of the result file `fin`.

For completeness the structures `geom`, `mat` and `bc`, created by the corresponding input files, are saved within the result structure as `fin.geom`, `fin.mat` and `fin.bc`.

To save further values simply embed them in the structure `fin`.

B.3.6 Plot results

By default, after the simulation has finished and the results are saved, chosen values are plotted to visualise the results:

- **Figure(2)** displays the normalised membrane water content.
- **Figure(3)** and **Figure(4)** display detailed results for the cathode and anode side, respectively. In the upper row from left to right, the mole fractions in the gas channel, the velocity in the gas channel and the average current density as well as potential of the fuel cell are plotted over time. In the bottom row the mesh plot represents the distribution of the GDL mole fraction.
- **Figure(5)** displays overall results of the fuel cell. In the upper row from left to right the first two plots represent the gas channel mole fraction for the anode and cathode side and the third plot displays the average current density as well as the fuel cell potential over time. In the bottom row from left to right the velocity and density for anode and cathode gas channels are plotted in the first two sub-plots and the distribution of the normalised membrane water content for the middle slice is displayed in the third sub-plot.

To view different instants of time, the slider bar of the figures can be used for adjustment.

B.4 Functions ^{DK}

The main functions used during the simulation are briefly described in this section to improve the code understanding. Additionally, several other short functions are used, e.g. for scaling the Gauß-Lobatto points from 0 to 1 (`scaledGaussLobattoPts.m`) or to compute commonly used constants in a pre-processing step (`helpVariables.m`). However, all functions, whether described here or not must not be changed by the user unless it is explicitly noted.

B.4.1 `SystemMatrix.m`

This function builds up the linear system of equations for the actual instant of time with the required boundary and coupling conditions included in the system matrix \mathbf{A} , see Eq. (3.5). To solve this system of equations the Matlab command `mldivide` is used.

B.4.2 `sliceCoupling.m`

For the opportunity to decouple the number of inner slices from the number of channel nodes, it is necessary to volume average the channel values and fluxes over the slice thickness and vice versa for a consistent coupling. As the equations should remain their almost fully implicit character this integration has to be embedded into matrix \mathbf{A} .

The function `sliceCoupling.m` creates the coefficients for the implicit integration, polynomial expansion and evaluation of the polynomial at the corresponding nodes, for more information see Sec. 3.3 and [33].

B.4.3 `central_diff_t.m`

The time derivative with respect to the current time step is built fully implicit with a scheme of second order in time $\mathcal{O}(\Delta t^2)$, Eq. (3.2).

Due to the linearisation with respect to the previous time step, the time derivative for the previous time step is also required, as shown in Eq. (3.4). Therefore, a central difference scheme of order $\mathcal{O}(\Delta t^2)$ is used to keep the equations as implicit as possible. For an arbitrary variable r the approximated time derivative reads:

$$\left(\frac{\partial r}{\partial t}\right)^{(n)} = \frac{r^{(n+1)} - r^{(n-1)}}{(1 + \alpha^{-1})\Delta t^{(n+1)}} + \mathcal{O}(\Delta t^2). \quad (\text{B.4})$$

During the computation this approximation is created by the function `central_diff_t.m`.

B.4.4 bc_physical.m

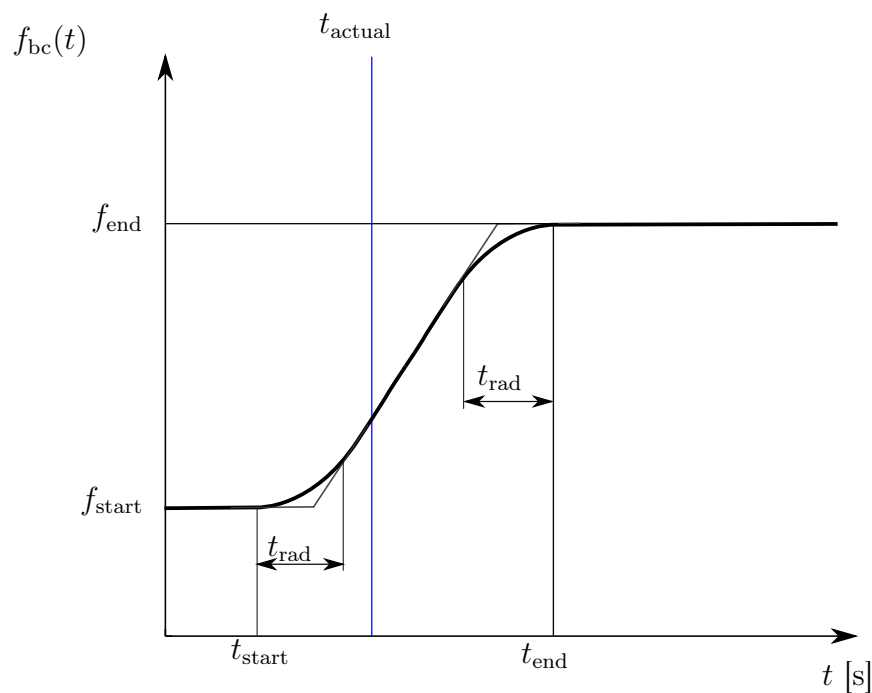


Figure B.6: Smooth function in time established with `bc_physical.m` with all necessary input parameters.

Since a change of physical quantities is never instantaneous in time, this function is used to create a continuously differentiable function $f_{bc}(t)$ for a boundary condition to be

changed. Starting from the start time t_{start} the initial value of the boundary condition f_{start} is varied in a smooth manner to reach the desired value of the boundary condition f_{end} at the time t_{end} . Moreover, the time radius to smear the function f_{bc} in time, see Fig. B.6, must be defined in the following order:

$$f_{\text{bc}}(t) = \text{bc_physical}(t_{\text{start}}, t_{\text{actual}}^1, t_{\text{end}}, t_{\text{rad}}, f_{\text{start}}, f_{\text{end}}) \quad (\text{B.5})$$

B.4.5 Chebfun package

The open source package chebfun [30] is used to build up the differentiation matrices and to provide the barycentric weights as well as the integration matrices used for integral coupling, see Sec. 3.3 in the `sliceCoupling.m` function, for more information see [33].

¹not to be changed